# Ground-bad Near-Infrarcd Observations of the Venus Night Side: The Thermal Structure and Water Abundance Near the Surface.

V. S. Meadows (University of Sydney and Anglo-Australian Observatory) and D. Crisp (Jet Propulsion Laboratory)

*VSM present affiliation: National Research Council Resident Research Associate, Jet Propulsion Laboratory.*

Abstract

We used ground-based near-infrared (NIR) observations of thermal emission from the Venus night side to determine the temperature structure and water vapor distribution between the surface and the 6 km level. We show that emission from spectral windows near 1.0, 1,1, and 1.18 $\mu$m originates primarily from the surface and lowest scale height ($\sim$16 km). These windows include absorption by weak $H_20$ and $CO_2$ lines and by the far wings of lines in strong nearby $CO_2$ bands. Rayleigh scattering by the 90-bar $CO_2$ atmosphere and Mie scattering by the $H_2SO_4$ clouds attenuates this emission, but adds little to its spectral dependence. Surface topography also modulates this NIR thermal emission because high-elevation regions are substantially cooler, and emit less thermal radiation than the surrounding plains. These contributions to the emission are clearly resolved in modelate-resolution ($\lambda/\Delta\lambda \sim 400$) spectral image cubes of the Venus night side acquired with the InfraRed imaging Spectrometer (IRIS) on the Anglo-Australian Telescope (A AT) in 1991 and 1993. To analyze these observations, we used a radiative transfer model that includes all of the radiative processes listed above. Synthetic spectra for several topographic elevations were combined with Pioneer Venus Altimetry data to generate spatially-resolved maps of the NIR thermal emission. Comparisons between these synthetic radiance maps and the IRIS observations indicate no near-infrarx!d signature of the surface emissivity differences seen at microwave wavelengths by the Magellan orbiter. Assuming constant surface emissivity in the near-infrared, we derive night-side averaged temperature lapse rates of 7 to 7.5 K/km in the lowest 6 km. These lapse rates arc smaller, and indicate much greater static stability than those inferred from earlier measurements and greenhouse models (8 to 8.5 K/km) [35]. The derived $H_2O$ mixing ratio profile depends on the assumed temperature lapse rate. If we assume a lapse rate near 8K/km, the $H_2O$ mixing ratio must decrease from $\sim$50 ppmv at the surface, to $\sim$25 ppmv at 16 km, and remain constant, between that altitude and the cloud base ($\sim$ 47 km). For temperature lapse rates < 7.5 K/km, a constant, water mixing ratio near 30 ppmv provides an acceptable fit to the data. '1'here is no evidence for $H_2O$ mixing ratios that decrease with altitude, like those inferred from Pioneer Venus Large 1 'robe Mass Spectrometer [1 5] or the Venera 11 and 12 Lander Spectrophotometers [28].

## 1 Introduction

The lower atmosphere of Venus extends from the planet's surface to the base Of the $H_2SO_4$ clouds (47km altitude). A better knowledge of the composition and thermal structure of this region is required to address several current problems in Venus atmospheric and surface

science. These include the origin and evolution of the Venus surface and atmosphere, the mechanisms which maintain the present-day greenhouse effect, aud the extent, of licar-surface momentum transports associated with the cloud-top atmospheric superrotation.

Because of its importance, many attempts have been made to study the lower atmosphere using a broad range of spacecraft aud ground-based obser vations. These investigations have provided constraints on the physical and chemical properties of this region, but have left several important questions unanswered. In particular, existing measurements have provided very little information on the thermal structure and composition of the lowest atmospheric scale-height (O 16 km). This region contains more than 60% of the mass of the atmosphere, and its physics] and chemical properties arc directly relevant to our understanding of interactions between the surface and atmosphere. The thermal structure in the lowest scale-height regulates the momentum transport between the surface and atmosphere, and may provide clues to the mechanisms which drive the atmospheric superrotation.

Our understanding of the greenhouse effect on Venus, which maintains the anomalously high surface temperatures, would also be improved by a better knowledge of both the thermal structure and composition of the lowest atmospheric scale height. The thermal structure can be used as a diagnostic to determine the efficiency of the greenhouse effect. A determination of the abundance of greenhouse gases, including water vapour and sulfur-bearing gases in the lowest atmospheric scale height, is also needed to assess the efficiency of this mechanism. Improved constraints on these properties would also constrain surface weathering rates, and place limits on the age of the Venus surface and atmosphere.

## 1.1 Previous Studies of the Lower Atmosphere

The lower atmosphere has been difficult to study for several masons. Optical investigations arc precluded by the planet-wide clouds. To penetrate this dense obscuration, observers have used either radio and radar measurements, or obtained measurements from entry probes which descended through the atmosphere.

Grouud-based radar, aud radar-equipped orbiting spacecraft, such as 1 'ioneer Venus and Magellan, provide exquisitely detailed maps of surface elevation and radar properties, but provide limited information on surface composition. For example, radar reflectivity and microwave emissivity maps of the surface have revealed dramatic variations in surface emissivity, which are associated with topography. Regions on the Venus surface with elevations of more than 5 km have much higher radar reflectivities, and correspondingly lower microwave emissivities, than the surrounding lowland plains [31]. These emissivity variations indicate a change in surface composition or texture, but these data provide insufficient information to determine the nature of these compositional changes.

Moreover, the weak interaction between radio waves and the atmosphere, which is so advantageous for mapping the surface, limits the amou nt of information obtained about the atmosphere. Spacecraft that descend into the lower atmosphere can tell us much more about the near surface region, but the hostile Venus conditions (730 K, 93 atm pressure at

the surface) constrain the lifetimes of descent craft to no more than an hour. In-situ probes also measure only their local environment, and spacecraft data on the lower atmosphere are consequently heavily restricted in temporal and spatial extent.

The Venera landers acquired only six measurements of surface temperature over a restricted area of the planet [35]. The atmospheric temperature measurements by these probes had inadequate vertical resolution to define the atmospheric temperature gradient near the surface. The Pioneer Venus probes produced a detailed description of the temperatures above 12 km, but their external temperature sensors failed at 12 km altitude on all four probes [36]. The Soviet VEGA-11 lander obtained the only high-resolution temperature measurements of the lowest scale height (0-16km) [42]. These measurements indicate a surprising amount of variability in the vertical temperature gradient, but their implications for the thermal structure and dynamics of the deep atmosphere are ambiguous because they provide no information about the temporal or horizontal variations in the temperature field.

Although many attempts have been made by entry probes to determine the water abundance and distribution in the lower atmosphere, the results are far from conclusive. Water concentrations measured by the Pioneer Venus and Venera entry probes exhibit a perplexing range from 20 to 5000 ppmv (see Tables 1 and 2, for a summary of water measurements to date. See Donahue and Hodges, 1992, for a complete discussion of water measurements up to 1992). Large latitudinal variations have also been claimed from entry probe measurements [34], but were not detected by ground-based observers [1 O]. Both the Venera results (from Veneras 11, 12, 13, and 14) and the Pioneer Venus Large Probe Neutral Mass Spectrometer indicate a decrease in water concentration from 20km altitude down to the surface [15, 29, 41]. However, the gradient observed by the Pioneer Large 1 'robe is now believed to have been affected by instrumental contamination [1 4]. If confirmed, this controversial gradient would require vigorous sources and sinks of water near the surface, and would affect not only estimates of the total water abundance in the lower atmosphere, but also our understanding of the chemistry and weathering of the Venus surface. These conflicting values and distributions of water vapor may reflect non-uniform spatial or temporal distributions of water vapor, which are sparsely sampled by current methods, or perhaps large measurement uncertainties. There is a clear need for a global study of water vapor to obtain a definitive total abundance.

## 1.2 Near-infrared windows: A new way of probing the lower atmosphere

The recent discovery of near-infrared windows in the Venus atmosphere [3, 2, 7] has provided a new means of probing the atmosphere below the cloud-deck. These infrared windows are found at wavelengths between strong $CO_2$ and $H_2O$ absorption bands in the Venus atmosphere, and within a spectral region where the sulfuric acid clouds are not strong absorbers (0.3 2.5 $\mu$m) [32]. Spectral windows have been detected at wavelengths near 1.0, 1.1, 1.18, 1.28, 1.31, 1.74 and 2.3 $\mu$m. The 1.74 and 2.3 $\mu$m windows reveal radiation that originates from below the cloud deck at 35-45 km altitude [1, 23]. These windows provide iufornla-

Table 1: Water in the Venus Lower Atmosphere - *In Situ* Spacecraft Results

| Mixing ratio (ppm) | Altitude (km) | Reference | Comments |
|---|---|---|---|
| ~300 | 42 | [27] | Veneras 9 and 10 |
| | | | Narrow-baud photometers |
| 200 | 52 | [29] | Veneras 11 and 12 |
| 150 | 42 | | scanning spectrophotometer |
| Go | 22 | | Linearly decreasing gradient infe |
| 20 | 0 | | |
| 76 | 0 | [21] | Venera 11 mass spectrometer |
| 67 | 22 | | |
| 130 | 0 | | Venera 12 mass spectrometer |
| 52 | 22 | | |
| ≤ 100 | <42 | [18] | Venera 12 |
| 200 | 40 48 | [28] | Veneras 13 and 14 spectrophotor |
| 20 ± 15 | 0 | | Linearly decreasing gradient infe |
| <1000 | <52 | [20] | Pioneer Venus Mass Spect. |
| | | | Preliminary results |
| 1350 | 22 | [30] | PV Lander |
| 5200 | 42 | | Gas Chromatograph |
| < 600 | 52 | | |
| 20 50 | ~ 40 | [34] | Near 600 latitude |
| 200 500 | ~ 40 | | Near 300 latitude |
| >500 | ~40 | | At equator |
| | | | PV infrared radiometer results |
| $67^{+44}_{-12}$ | 10 25 | [15] | PV LNMS results - Measure] |
| $17^{+16}_{-6}$ | 0 | | non-linear decreasing gradient |
| 43 | 10 25 | [14] | Reanalysis of PV LNMS results |
| | | | Possibly uo gradient |

'1'able 2: Water in the Venus Lower Atmosphere - Ground-Based and Flyby Remote Sensing

| Mixing ratio (ppm) | Altitude (km) | Reference | Comments |
|---|---|---|---|
| $25^{+25}_{-13}$ | 30 35 | [7]---- ' | Galileo NIMS 2.3 $\mu$m window |
| $50^{+50}_{-25}$ | 20 28 | [7] | Galileo NIMS 1.74 $\mu$m window |
| 30 ± 15 | 5 20 | [16] | Galileo NIMS 1.18 $\mu$m window -over 40° S to 50° N latitude - Spatial variations < 20% - Constant gradient |
| ~ 20 | < 48 | [6] | Ground-based obs. below |
| 34 ± 10 | <48 | [12] | |
| 40* 20 | < 48 | [10] | Spatial variations < 10% at 30 45 km |
| 40 | < 55 | [4] | large horizontal Variation observed |
| 200 | <40 | | |
| 30 ± 15 | < 48 | [13] | |
| 30 ± 6 | 23 47 | [32] | possible negative gradient |
| 30+ 7.5 | 14 35 | | |
| 30* 10 | 5 19 | | |
| 3.5 15 | 0 | | |

tion about the composition and physical properties of the atmosphere just below the Venus clouds (25 45 km). Spectroscopic analyses within these windows [32, 10, 13, 23, 22, 7] have provided improved constraints on the abundances of trace constituents such as $H_2O$, HDO, OCS, $SO_2$, HCl and HF at these altitudes.

The shorter wavelength windows at 1 .0 1.3pm permit observation of thermal emission from even deeper within the Venus atmosphere. Theoretical radiative transfer models [1 O, 32] indicate that a large fraction of the radiation within the 1.0 1.18 $\mu$m windows originates from the Venus surface. Ground-based spectra within these windows have been taken at isolated regions on the Venus night-side [1 O, 32, 13] and have been used to infer the $H_20$ abundance thoughout the lower atmosphere. These studies indicat e that the $H_2O$ abundance is near 30 ppm, but these data provide very weak constraints on the horizontal distribution of this gas. These observations also do not have adequate vertical resolution for studies of the water distribution in the lowest scale height, partly because the sensitivity function for water in the lower atmosphere is broad, and peaked well above the surface [32], Individual observations of water absorption can therefore be modelled by multiple combinations of water abundances and gradients [32]. In spite of these limitations, these measurements indicate substantially less water than the Pioneer Venus observations (~ 100 ppm)

The Galileo Near Infrared Mapping Spectrometer (N I MS), which flew try Venus in February 1990 [7], obtained high spatial resolution (1 1-50 km)/low spectral resolution (~40) spectral mapping cubes within all known near-infrared windows. Spectra from these cubes have been used to obtain estimates of the water abundance within the 2.3 and 1.74 micron windows, corresponding to 30 35 and 20 28 km altitude. Water concentrations of 25 and 50 ppm were measured at these altitudes, with errors conservatively estimated to be +1 00% and – 50% of these values. NIMS data obtained within the 1.18 $\mu$m window []6], show values

for the lower atmosphere water abundance of 30 $\pm$ 15 ppm, consistent with the values obtained from ground-based observations. In addition the NIMS results show no apparent $H_2O$ spatial variations exceeding 20%, nor do they detect variations in column abundance with topography, although it is argued that $CO_2$ continuum opacity would prevent the probing of altitude levels deeper than 2 km [1 6].

The work presented in this paper describes the first ground-based attempts to use spatially resolved spectroscopy to undertake a global exploration of the surface and lower atmosphere of Venus within these newly discovered windows. The goals of this project were to:

1) Observationally confirm model predictions that emission originating from the Venus surface could be detected within the 1.0, 1.1 and 1.18 $\mu$m windows. 2) search for infrared emissivity changes correlated with topography 3) determine the global thermal structure of the lowest 6 km of the atmosphere, and 4) determine the global water abundance and gradient in the lowest 6km of the atmosphere.

To achieve these goals, spectral mapping data have been analysed with models which combine Pioneer Venus altimetry data with sophisticated radiative transfer codes to produce synthetic radiance spectra and maps of the Venus night-side. These results introduce new methods of obtaining information on the Venus lower atmosphere and place important new constraints on the spatial distribution and abundance of near-surface water, surface emissivity and atmospheric temperature profiles.

## 2 Observations

The data used for this study were taken with the Infrared Imaging Spectrometer (IRIS) on the Anglo-Australian Telescope (A AT) both before and after the August 1991 inferior conjunction. However, the principal data analyzed in this paper were taken on UT 27 July, 1991. A summary of all observations is shown in Table 3.

The IRIS detector is a 128 x 128 format HgCdTe (NICMOS2) array, manufactured by Rockwell International. For this work IRIS was configured to take spectra with a resolution of $\sim$ 40() ($\lambda/\Delta\lambda$), where $\lambda$ is wavelength. A slit of 1,4" x 12" was oriented in the East-West direction. To produce spectral image cubes of the Venus night-side, a series of spectra were taken while the telescope was scanned in the North-South direction, perpendicular to the slit. At least one complete South-North-South pass was made in order to average fluctuations in seeing and changing sky brightness. The telescope drift rate was set such that 0.8" (the pixel size used) were covered in the time for each spectral integration, which for the July data, was 2 seconds at each scan position. This ensured square 0.8" pixels on any image produced by this method. These image cubes contain information in two spatial dimensions (along the slit and in the scan direction) and one spectral dimension (orthogonal to the spatial dimensions). The wavelength range covered was ().9 1 .33$\mu$m, with a spatial pixel size of 0,8". However, terrestrial seeing of $\sim$ 1" limits our spatial resolution to $\sim$ 250 km at the sub-Earth point on Venus.

Table 3: Table Of Venus Observations

| UT date 1991 | ZD (degrees) | apparent diameter (arcsec) | apparent diameter (pixels) | illuminated phase (%) | radial velocity ($km\ s^{-1}$) |
|---|---|---|---|---|---|
| Jul 27.35 | 69 | 44 | 56 | 18 | --10.2 |
| Jul 28.35 | 69 | 45 | 57 | 17 | --10.0 |
| Sep 17.02 | 41 | 45 | 57 | 17 | 9.1 |
| Sep 19.85 | 61 | 44 | 56 | 18 | 9.6 |
| Sep 19.90 | 49 | 44 | 56 | 18 | 9.6 |
| Sep 20.85 | 62 | 43 | 54 | 19 | 9.8 |
| Sep 20.91 | 47 | 43 | 54 | 19 | 9.8 |
| Oct 17.79 | 67 | 30 | 38 | 41 | 12.4 |
| Oct 18.79 | 68 | 29 | 37 | 41 | 12.4 |
| Ott 19.79 | 68 | 29 | 37 | 42 | 12.4 |

Measurements of the sky were obtained by scanning beyond either side of the planet in the S N scan direction. In the E-W direction the images are restricted by the usable slit length to 12". Several overlapping scan strips were therefore required to map the entire Venus disk. Due to adverse weather conditions on 27 July, 1991, only two scan strips were taken, covering some 50% of the Venus disk. However, the July data were used in preference to the others, as they were taken on a dark sky. All other observations were taken in daylight, when scattered sunlight from the terrestrial sky precluded observations of Venus atmospheric windows shortward of the 1.18pm window. All observat ions were taken as close to inferior conjunction as possible when the apparent diameter of Venus is larger, and increases our potential spatial resolution. In addition, close to inferior conjunction the fraction of the Venus disk that is sunlit is relatively small, reducing contamination of the data by scattered light, and allowing observations of large areas of the Venus nightside.

# 3 Data Processing Steps

The raw data cubes were initially processed to correct for the non-linear response of the data system to incident radiation. Once linearized the cubes were 'folded' by registering and coadding the S— N and N – S passes produced by the drift scanning procedure. The folding process combines all exposures of the planet, and reduces the size of the cube, consequently reducing the computer processing time for subsequent data-reduction steps. Standard spectral reduction techniques are then applied to each spectral plane of the coadded cube. These techniques involve correcting for the spectral and spatial response of the detector, straightening the curvature of the echelle orders as displayed on the detector, and correcting for the rotation of the slit position, which changes across the orders [25].

once the instrumental response has been removed by the above steps, several spectral planes are extracted from positions in the cube where the sky was observed. These planes

arc averaged and then subtracted from each spectral plane in the data cube to remove the background sky level in the spectra.

Scattered light from the bright sunlit crescent is removed individually for each pixel in the image plane of tile cube. First, a spectrum of the crescent is extracted from unsaturated regions of the crescent in the data cube. This template crescent spectrum is then normalized individually to each data spectrum using sections of the spectrum within strong $CO_2$ absorption bands. in these regions (outside the windows) the Venus atmosphere is assumed to be opaque to upwelling thermal radiation and only scattered radiation from the crescent is observed. Once individually normalized, the crescent spectra are subtracted from the corresponding data spectra. A wavelength scale, derived from arc lamp measurements, is then added to the data.

Given the high airmass of these observations, using a photometric standard star to remove terrestrial absorption lines is problematical, as that star would have to be observed at the same airmass as the data. As an alternative, we used a template crescent spectrum, whose continuum was forced to match the counts and spectral shape of a photometric standard star (13 S5384, a G3V). The resulting hybrid star/crescent spectrum retains a record of the terrestrial absorption lines at an identical airmass to the data (as the crescent spectrum is extracted directly from the data cube), and can also be used as a photometric standard for the data. The data were flux-calibrated using the hybrid star/c. rescent spectrum, and were further corrected for an estimated 17% light loss from the placement of the standard star on the slit. The intensity of the long wavlelength side of the 1. 18$\mu$m window was compared to values obtained from spectra taken near the sub-Earth point for two independent observations of the 1.18 $\mu$m window: one from observations made in 1990 using the Far Infrared Grating Spectrometer (FIGS) on the Anglo-Australian Telescope, and the other from observations taken in 1 991 with the Fourier Transform Spectrometer (h'T'S) on the Canada France Hawaii Telescope. The threw data sets agree to within 10%, and our calibration for the IRIS cubes is believed to be accurate at that level. All the processing steps described here arc presented in more detail in Meadows, 1994 (Ph.D. thesis) [25]. An example of a fully reduced IRIS spectrum of the Venus night-side is shown in Figure 1.

# 4 Sources of near-infrared contrast observed within the atmospheric windows

Images of Venus taken within near-inframd windows show bright and dark features on the Venus lliglltl-side [3, 1 O]. This radiation originates as thermal emission from the surface and lower atmosphere. 1 lowever, the contrasts in this emission can be produced by a number of processes, including cloud opacity, surface or atmospheric temperature variations, surface emissivity variations, and spatial variations in absorbers. As radiation from below the clouds escapes upwards, it passes through different scattering optical depths in the $H_2SO_4$ clouds. The resulting differences in transmission produce large-s(:alc bright and dark markings on the Venus night-side. Cloud-contrast features arc present in all the near-infrared windows, but

the contrast increases with increasing wavelength, and these features are most apparent in images taken within the 2.3$\mu$m window. However, as will be demonstrated in this paper, the radiation observed within the 1.0, 1.1 and 1.18 $\mu$m windows contains a large component of surface thermal emission. Consequently, surface topography can modulate the near-infrared thermal emission observed. High-elevation surface regions are substantially cooler and therefore emit less thermal radiation, appearing darker than the surrounding plains on infrared images. Variations in near-infrared surface emissivity, like those inferred from the Magellan radar measurements, would also produce contrasts in tile observed 1 R emission, with low surface emissivity regions appearing darker than a surface region of comparable elevation that had a higher surface emissivity. Finally, The 1.1 and 1.18/m windows include absorption from weak $H_2O$ lines. Spatial variations in water abundance along the line of sight will produce spatial contrasts in the observed infrared emission within these windows.

# 5 The Models

To analyze the IRIS spectral mapping observations, wc have used sophisticated radiative transfer models of the Venus atmosphere. The models usc an assumed set of atmospheric parameters to produce synthetic spectra of radiance (observed intensity, measured in W $m^{-2} sr^{-1}$) as a function of wavelength (in $\mu$m). To model realisticall y the observed radiation as a function of wavelength for a planetary atmosphere, physical processes such as multiple scattering by gases and aerosols, thermal emission and absorption within a vertically inhomogeneous medium, and emission and scattering at the planet's surface must also be included.

The SMART (Spectral Mapping Atmospheric Radiative Transfer) model, developed by one of us (DC), incorporates all the physical processes described above and provides the high spectral resolution synthetic radiance spectra of the Venus atmosphere which were used to analyst the observed spectra extracted from the IRIS data cubes. To analyse the images extracted from the IRIS data cubes. The program VENRAD was developed by one of us (VSM ) to combine the SMART synthetic radiance spectra with information on surface altitude and viewing angle to produce synthetic radiance maps of Venus for a given date of observation. SMART and VENRAD arc described in more detail below.

## *5.1* S M A R T

The SMART code provides numerical solutions to the equation of transfer using the discrete *ordinate method* [37]. This method provides an angle-dependent solution for each of 50 levels of the Venus atmosphere. After testing, it was found that eight discrete zenith angles (four up and four down), and a single azimuth angle, were adequate to describe the radiance field to an accuracy of $\sim$ 2%. For the results presented here, radiances were determined at, the Gaussian quadrature points in the upper hemisphere, at zenith angles of 21.48, 47.93, 70.73 and 86.02 degrees.

The input parameters to SMART include t ie atmospheric thermal structure $T(\tau)$, and

the atmospheric optical properties, the optical depth, $\tau$, the single-scattering albedo, w, and the scattering phase function, $P$. The atmospheric optical properties are determined by the composition and physical conditions within the atmosphere. Within each of the 50 atmospheric layers in the model, w and $P$ are assumed to be constant, and $B[T(\tau)]$ is assumed to vary linearly with $\tau$. The surface boundary condition is characterized by an albedo, $a$, and a surface reflection function $P_a(\mu, \mu')$. The top boundary condition is specified as a downward flux at the top of the atmosphere. For night-side calculations, both the downward solar and the thermal fluxes as set to zero at this level. The optical properties of the atmosphere are derived by summing the contributions from each constituent of the atmosphere. For Venus, these atmospheric constituents include gaseous $CO_2$, $H_2O$, CO, OCS, and $H_2SO_4$ aerosols. Aerosol scattering properties are derived from a Mie scattering algorithm [40]. The scattering by gases in the Venus atmosphere is approximated by Rayleigh scattering. Because the Rayleigh scattering cross-section decreases as the fourth power of wavelength, this source of extinction is normally important principally at ultraviolet and visible wavelengths. 1 lowever, in the deep, high-pressure atmosphere of Venus, the column-integrated optical depth due to Rayleigh scattering exceeds unity near wavelengths as great as 1.1 $\mu$m, and this process is included in the mode] at all wavelengths.

The gas absorption optical depth at a given wavelength is given by the sum of all contributions by gases that absorb at that wavelength. The optical depth contributed by a given absorbing gas is proportional to the product, of the gas absorption cross section per unit molecule and the number density of that molecule, integrated over the optical path. The number density of a given constituent is given by the product of the ambient number density of the atmosphere and the volume mixing ratio of that gas.

For simulations of the atmospheric windows in the wavelength range 1.0 1.32 $\mu$m the HITEMP spectral line database for $CO_2$ [39, 32] was used. This database provides improved results compared with previous databases (such as HIT I{ AN) as it includes a more complete set of weak overtone bands and hot bands which produce significant opacity in the relatively high temperatures and pressures of the Venus lower at mosphere. The HITRAN database was used for the $H_2O$ and $HCl$ and HF band parameters. For $H_2S$ we used a new spectral line database compiled by Linda Brown of JPL (personal communication, 1993).

Atmospheric pressure and temperature profiles were obtained from the Venus International Reference Atmosphere, and a $CO_2$ volume mixing ratio of 0.965 was assumed at all levels. Estimates of nominal mixing ratios for $H_2O$, HF and $HCl$ were obtained from previous ground-based observations [5, 12, 32]. The distribution of $H_2SO_4$ cloud aerosol particles was based on models derived from Pioneer Venus and Venera entry probe measurements. Two cloud models were used to analyse the data here. The principal model was developed to fit spectra obtained by FIGS on the AAT [1 O], and the second was developed to fit the Pioneer Venus data [9].

Except when altered to investigate the effect of surface emissivity changes, a nominal surface emissivity of 85% is assumed. Intensities were Calculated at (), 2, 4 and 6 km surface elevations. The model was also run for ranges in surface emissivity and cloud transmission, To determine the water abundance in the lower atmosphere, a range of water abundances

(e.g. 15, 20, 30 and 60 ppm) and $H_2O$ gradients in the lower at mosphere was used.

The output of this model is a binary file containing tile model radiances for each of the 4 upward streams as a function of wavenumber, for the choice of values for altitude, emissivity, water abundance and cloud transmission. An example of SMART synthetic radiance spectra is shown in Figure 2.

## 5.2 VENRAD

For many of the applications described here, e.g. detection of emission from surface topography, and the spatial distribution of water in the lower atmosphere, it is necessary to produce models which contain spatial information about the predicted intensities of infrared radiation. The program VENRAD was written specifically for this purpose.

VENRAD creates a model map of the infrared emission from the surface and atmosphere of Venus on a given observing date. Variations in optical depth in the Venus clouds are not modelled, so that any cloud optical depth variations must be corrected for in the data before comparison with the model. As input, VENRAD requires a digitised altimetry map, and a series of synthetic spectra generated as a function of altitude and viewing angle. The model spectra are provided by SMART. VENRAD currently uses the altimetry map produced by the Pioneer Venus orbiter. Given the sub-Earth latitude and longitude (i.e. the planetary latitude and longitude of the center of the disk of Venus, as observed from Earth), the model determines the surface elevation and sub-Earth angle corresponding to each pixel on the IRIS image.

The angle and altitude dependent, synthetic radiances derived from SMART are then interpolated to these coordinates. The output files from SMART include 4 viewing angles, and several altitude values (typically, O, 2, 4 and 6 kin). A hi-cubic spline is used to interpolate a four by four grid of intensities over the altitudes and viewing angles. These interpolated radiances are then mapped to the output image. The interpolation can be done over any user-specified wavelength range and this is particularly valuable when creating spatial maps of radiance within water absorption lines.

As options, VENRAD will also plot the terminator line, or the extent of the sunlit portion of the planet at the time of observation, providing a realistic simulation of the crescent phase expected in the observations. An example of a synthetic radiance map produced by VENRAD is shown in Figure 3.

# 6 Results

## 6.1 Detection of Infrared Contrasts due to Surface Topography in the 1.0, 1.1 and 1.18pm windows

**'1'0** constrain the thermal structure and composition of the deep atmosphere, the spectra] windows at 1.0, 1.1 and 1.18 $\mu$m must be sufficiently transparent to allow thermal radiation to escape from the surface. Images of intensity contrasts that are spatially coincident with topographic features have previously been published ([26, 24, 8]), and strongly suggest that the emission in these windows originates from the surface. However, as outlined in section 4, several phenomena could contribute to the observed radiance contrasts. For example, the possibility that features observed are due to opacity variations in the Venus cloud-deck, rather than the surface itself, must be eliminated before a surface detection can be proven.

Here we combine multi-wavelength observations with sophisticated radiative transfer models to prove that we see infrared contrasts due to surface topography in the 1.0, 1.1 and 1.18$\mu$m windows. The observational arguments presented are based on our understanding of the thermal structure, optical properties, and dynamics of the Venus atmosphere. We also provide the first estimates of the relative contribution of the surface emission to the total radiation observed within these windows.

### 6.1.1 Distinguishing Surface From Cloud Contrasts

If the atmospheric temperature lapse rate in the lowest scale height is $-8$K/km [35], and the surface temperatures are comparable to the atmospheric temperatures as the same elevation, then high-elevation surface regions will be much cooler than the surrounding plains. These higher, cooler regions will therefore emit less thermal radiation, and will appearing dark on an infrared image. These contrasts would be expected to spatially correlate with surface topography. Radiative transfer modelling also indicates that the emission contrast between high and low altitude should increase with decreasing wavelength, being more pronounced in the 1.0 $\mu$m window.

Cloud induced contrasts associated with the main cloud deck behave in the opposite fashion, by decreasing with decreasing wavelength. The contrast between dark and bright markings at 2.3 $\mu$m exceeds a factor of 5, compared with contrasts of 0.3 at 1.27 $\mu$m [10]. Here contrast, C, is defined as:

$$C = \frac{b_1 - 02}{b_1} \quad (1)$$

where $b_1$ and $6_2$ are observed intensities. However, in the 1.0 to 1.27 $\mu$m range, radiative transfer modelling suggests that the amplitude of the cloud induced thermal contrasts decreases very little. For example, for the 112S04 cloud particle imputations specified by

Crisp (1 986), and optical depth contrasts like those described by Grinspoon *et* al. (1993), the thermal contrast varies from 0.3 at 1.27 $\mu$m to about 0.285 at 1.0 $\mu$m.

Another distinguishing feature is that cloud-induced contrasts arc known to rotate with a 5 to 6 day period [1 1]. In comparison, contrasts associated with surface features would rotate with the planet's surface, some 40 times slower than the cloud features.

Figure 4 shows the sequence of images extracted from a single IRIS data cube within the 1.31, 1.27, 1.18, 1.1 and 1.0 windows. For comparison, an altitude map created by VENRAD is also shown, depicting the topography of the Venus surface on the date of the observations at IRIS pixel resolution. On this map higher altitude regions arc darker than the lowlands.

In Figure 4, the 1.31 and 1.28 $\mu$m images arc dominated by contrast markings due to horizontal differences in cloud opacity, also seen in 2.3 $\mu$m images t aken on the same day. The 1.28 $\mu$m image also contains emission from the $O_2\,^1\Delta$ 1.269 $\mu$m band, which in this case most noticeably boosts the radiation seen near the Easter n iimb (cf. Figure 1 of Crisp *et* al., 1995, this volume). Cloud induced contrasts arc also clearly visible in the remaining windows, including the 1.0 $\mu$m window, but an additional dark feature on the northern hemisphere is seen near the crescent. The contrast of this feature increases at shorter wavelengths, being icss obvious in the 1.18 $\mu$m image, but clearly visible in the 1.0 $\mu$m image. The position of this dark feature corresponds exactly to the geographical location of the highland region Beta Regio, seen as the large dark oval on the altimetry map.

Figure 5 shows 1.18 $\mu$m images taken on 1991 October 16, 17 and 18 (UT). At this time Venus was well past inferior conjunction with a phase of $\sim 0.4$ and an apparent diameter of only $\sim$ 30". It was therefore observed at a much lower spatial resolution. A dark feature parallel to the equator maintained its position over the t hrcc consecutive days of observing. Aiso shown arc 2.3 $\mu$m images which illustrate the horizontal variation of optical depth in the cloud layer. The cloud pattern changed markedly over the three days of observing, so it is unlikely that the dark feature is cloud-related. Also shown arc altitude maps for the dates of observation, showing the position of the equatorial highland region Aphrodite Terra, and its relative movement over the period of the observations. It can be seen from this diagram that the position of the dark feature observed in the 1.18 $\mu$m images corresponds closely to the geographical location of Aphrodite Terra.

Our infrared data arc coincident with those taken by Lecacheux *et al.* at 1.0$\mu$m with an optical CCD camera during the period 12 to 21 October, 1991. They also saw contrasts in emission apparently produced by the high altitude topographic feature Aphrodite Terra, with a high degree of spatial correlation between observed emission and surface elevation. Moreover, Lecacheux *et al.* claim that the individual CCD images used to create the published composite CCD image showed a rotation period consistent with the dark features observed being produced by the surface.

IRIS data were also obtained in the 1.18 $\mu$m window in September 1991, but show no obvious features, other than cloud induced contrasts. Comparison with the altitude map created for these observations shows that no large regions of high topography were visible 011 these dates.

### 6.1.2 Removing Cloud Contrasts

'1'0 strengthen the evidence that the oval feature observed in the July IRIS data (Figure 4) was due to a surface feature, the 1.0 and 1.18 micron images were divided by a scaled, limb-corrected image of the cloud contrasts observed in the 1.31 $\mu$m windows (Figure 6). This method removes most modulation of emission by the cloud opacities, leaving only the true contrasts of emission from the lower atmosphere and surface. The resulting 'cloud-removed' images arc shown in Figure 7. For comparison, two VENRAD synthetic radiance maps were produced within the same wavelength region as the data. These maps show the infrared radiances expected from the surface and atmosphere for uniform cloud opacity and surface emissivity. '1'0 compare contrasts observed in the model and data, small apertures were placed on and off Beta-Regio to derive contrasts as defined by Equation 1 of 0.26+ 0.04 for the data and 0.29 ± 0.02 for the model in the 1.18 $\mu$m window. The errors are derived from the standard deviation within each aperture. The standard deviation has two sources in the data, the variation of surface altitude within the aperture, and noise sources in the data, whereas the model error comes only from the variation of altitude within the aperture.

Note also that surface elevation differences of 1 km above the plains are clearly visible in these images. This implies that not only are we seeing contrasts in thermal emission from surface topography within the 1.0, 1,1 and 1.18 $\mu$m windows, but that we do indeed probe right to the surface of the planet.

### 6.1.3 Relative Contributions of Surface and Atmospheric Emission withing the 1.0, 1.1 amd 1.18 $\mu$m windows

To derive quantitative information on the relative contribution of surface emission within these windows we attempted to model this emission with a radiative transfer model. Although comprehensive radiative transfer models like SMART cannot provide conclusive proof that we arc seeing the surface, it seems highly unlikely that such a model could provide a good fit to the observed spectrum of the Venus night-side if the assumed abundance and vertical distribution of the atmospheric constituents, and the contribution to the emission from the surface, was grossly in error. An example of the SMART synthetic radiance spectra of the Venus night-side is shown in Figure 8. The two spectra indicate the emission expected with and without the surface thermal contribution. When surface thermal emission is included (solid line), the spectra obtained arc very similar to the IRIS observations (cf. Figure 1). When the surface contribution to the observed radiation is removed, and only the thermal contribution from the atmosphere is considered, the spectra do not look like the data, with the most notable difference being observed in the 1.0 $\mu$m window. Comparison of the spectra obtained with (solid line) and without (dotted line) the surface thermal contribution indicates that in the atmospheric windows below 1.27$\mu$m, a large fraction of the radiation observed (> 50%) will be due to surface thermal emission. The surface contributes little or no emission in the 1.28 and 1.31$\mu$m windows, between 60 40% of the emission in the 1.18$\mu$m and 1.1 $\mu$m window, and virtually all (> 95%) of the radiation observed within the 1.0 $\mu$m window.

'] 'hese theoretical estimates of the contribution to the observed thermal emission by the surface should be compared with the contrast features seen within the windows in Figure 4. The oval feature, Beta Regio, cannot be seen within the 1.31 and 1.27 $\mu$m, where the synthetic spectra predict little or no contribution from surface emission. As we move to shorter wavelengths, Beta Regio first appears at low contrast, in the 1. 18$\mu$m window, and increases in contrast with decreasing wavelength, until it is most prominent in the 1 .() $\mu$m window, as expected from the synthetic radiance spectra. These results, and the other arguments presented at the beginning of this section, strongly suggest that we detect radiation from the Venus surface and lower atmosphere from within the 1.0, 1,1, and 1. 18$\mu$m windows.

## 6.2 **Near-infrared Surface Emissivity Variations**

As variations in the opacity of overlying cloud will smear and confuse the relationship between surface emission and topographic elevation, cloud-induced contrasts in the observed emission were removed as described in section 6.1.2. The resulting images arc used for a quantitative study of surface emission.

To search for variations in surface emissivity as a function of surface elevation, the cloud-corrected data were divided by a synthetic radiance map that was created with a uniform surface emissivity ($\epsilon$ = 85%). The maps are shown in Figure 9. The upper image shows the cloud-corrected 1.18 $\mu$m image divided by the synthetic radiance map. For comparison, the synthetic radiance map is shown in the lower image. On inspection, the data/model division image shows a faint negative image of the cloud pattern, indicating a slight over compensation in the cloud-corrected image. No obvious features that are correlated with topography, or t he observed radar bright regions are seen, and they would be expected if surface emissivity was anomalous on high altitude regions like Beta Regio. To quantify this, small apertures were place over Beta Regio and the nearby plains region, and the mean value and standard deviation within these apertures was recorded. Contrast is defined by Equation 1 such that identical intesities produce zero contrast. The measured contrasts were $0.26 \pm 0.04$ for the cloud-corrected 1.18 $\mu$m image, and --0.03+ 0.04 when that cloud corrected image is divided by the synthetic radiance map. Thus, by assuming a constant surface emissivity, we have accounted for about 90'% (and possibly all) of the contrast observed between the 4 km high Beta Regio and the O km plains. We therefore find no infrared signature of the large variations (20 50%) in the surface emissivity seen at microwave frequencies [31]. Note also that the model used for the comparison has a lapse rate (– 7.5 K/km) that is mom stable than has previously been assumed (see below), and if anything we have *underestimated* the intensity of the highland regions in the model, resulting in a sign change in the contrast. To allow an anomalous decrease in the emissivity of the highlands in the sense of the microwave observations, the thermal gradient in the lower atmosphere would have to be even shallower, requiring a lapse rate that is even more stable than we have assumed. Consequently, a constant, surface emissivity was assumed in all further analysis presented here.

## 6.3 The Temperature Structure of the Lowest 6 km of the Venus Atmosphere

The atmospheric region which extends from the surface to a few km altitude is known as the planetary boundary layer. Knowledge of the thermal structure of this layer is essential for studies of the Venus global circulation, because the stability of the planetary boundary layer regulates the transport of heat, mass and momentum between the planet's surface and the atmosphere.

If the planetary boundary layer is relatively stable, atmospheric flow over the surface is more laminar, and there is very little transfer of surface angular momentum to the horizontal winds. However, if the near-surface atmosphere shows convective instability, horizontal momentum is effectively transport vertically through the planetary boundary layer, maximising the vertical extent of the atmospheric region affected by the surface drag.

The stability in the near surface atmosphere can also play an important role in the transfer of momentum to much higher layers of the atmosphere by vertically propagating waves. For example, waves that are produced when the wind blows over mountains and other topographic obstacles can propagate as far as the upper troposphere ($\sim$60 km altitude), transporting both heat and momentum. Young *et* al. [1987] have shown that if the lower atmosphere is stable, then these topographic waves can interact with the superrotation at the cloud level to produce a drag. '1'heir effects are dramatically reduced if the lower atmosphere is only marginally stable, or adiabatic.

Prior knowledge of the thermal structure of the near-surface boundary layer is required to derive the abundance of water, and other absorbers in the near-surface atmosphere from near-infrarccl observations of the Venus night-side. The effect of uncertainties in the vertical temperature gradient on the retrieved water vapour distribution is described in the next section.

Finally, a comprehensive *global* description of the near -surface thermal structure is essential to assess the efficiency of the Venus greenhouse mechanism. The Venus greenhouse is maintained primarily by the absorption of infrared radiation by $CO_2$. However, water, $S0_2$, and $H_2SO_4$ play an important role by absorbing in complementary regions of the spectrum, and effectively 'plugging' holes in the greenhouse left between the strong $CO_2$ absorption bands. Previous models of the Venus greenhouse have required 100 1000 ppm of water in the lower atmosphere, and an unbroken cloud deck [33]. However, recent uear-infrared observations, including the results presented here, have shown partial clearings in the $H_2SO_4$ clouds, and water abundances of only 30 pprn in the lower atmosphere. On their own, these observations would suggest, the existence of radiative 'leaks' in the Venus greenhouse and weaken the ability of current models to explain the high surface temperatures, and the efficiency of the Venus greenhouse. However, these apparent losses in efficiency of the greenhouse models, may be offset by the other sources of absorption that were neglected in these models. For example, ncw spectral line clata-bases for $CO_2$ and water include previously omitted hot-band lines, that arc important sources of opacity in the Venus lower atmosphere. Global observations of thermal structure as a function of local t imc could be used to constrain the

efficiency of the greenhouse mechanism. If the troposphere is truly opaque to thermal radiation, virtually all of the heat must be transported vertically by convection, and the lapse rate should be close to adiabatic. If both convection and radiative cooling are occuring, due to "leaks" in the greenhouse, then a more stable temperature lapse rate would be possible.

To derive the thermal structure of the lowest 6 km of the atmosphere, we assume that for the massive, high heat capacity Venus atmosphere, the atmospheric temperatures at the surface are equal to the surface temperature. With this assumption the temperature lapse rate can be derived by comparing the observed thermal emission as a function of surface elevation with model results for a variety of temperature lapse rates.

However, as both thermal structure and water concentration affect the observed emission gradient, to accurately determine the thermal structure, a region of the spectrum must be chosen which is unaffected by water. Images for comparison with the models are therefore extracted from within the long-wavelength side of the 1.18 $\mu$m window, which is dominated by $CO_2$ absorption, and where water absorption is negligible. The region 1.1904- 1.2003 $\mu$m was used to create the data and model maps used in the following analysis.

The synthetic radiance maps were created using VENRAD. The IRIS map was then divided by the synthetic map to produce a ratio image. This image was then binned as a function of altitude and local time. Synthetic maps were created for the Venus night-side with temperature lapse rates of –8.5 K/km (super-adiabatic) and --7.5 K/km (more stable). The model/data ratios for these lapse rates are shown as a function of local time in Figures 10 and 11.

If the model was a perfect match to the data, the data/model ratio would be a horizontal line at a ratio value of unity. It is clear from these plots, that within the wavelength range used to create the images, the model overestimates the observed intensity. However, this only affects the vertical position of the line on the plot, and will not affect the slope of the line, or the derived lapse rate. It should also be noted that the local time range 20-21 hrs produces inferred lapse rates that are far smaller than those derived for other local time regions. These results however, may be strongly affected by scattered radiation from the sunlit crescent, as the 20 21 hrs region is adjacent to the crescent. The best match to the slope for the remainder of the local time range is given by the --7.5 K/km lapse rate, with some indication that an even smaller lapse rate is required.

Given that the adiabatic lapse rate for the planetary boundary layer is calculated to be –8.3 K/km [36], a value for the observed temperature lapse rate of 7- 7.5 K/km implies far greater stability at these levels than was assumed previously. This would indicate that radiative, as well as convective cooling, is important in the lower atmosphere, and suggests the possibility of radiative leaks in the Venus greenhouse. The greater stability would also have important implications for the extent of vertical transport of momentum via gravity waves, as these waves propagate more readily through stable conditions.

The results derived in this section are also important when determining the abundance and distribution of absorbing components in the atmosphere, as differences in absorber column depths, and changes in the observed lapse rate can produce similar effects on the

observed infrared emission. Since we derived the temperature lapse rate from a spectral region where $CO_2$ was the only significant absorber, the derived lapse rate can now be used to infer the abundance and distribution of trace species, such as water vapor.

## 6.4 Water Abundance and Spatial Distribution in the Lower Atmosphere

The long-wavelength side of the 1.18 $\mu$m window is sharply defined by far-wing absorption from a $CO_2$ band near 1.205 $\mu$m. The short-wavelength side of this window also contains contributions from $CO_2$ absorption, but is dominated by absorption from the $\nu_1 + \nu_2 + \nu_3$ band of water vapour, centred near 1.1351 $\mu$m. Several other individual water lines are visible in the window shortward of 1.185 $\mu$m [13]. The long-wavelength side of the 1.1 $\mu$m window is similarly affected by water absorption. Our radiative transfer model results demonstrate that the entire region spanning the long-wavelngth side of the 1.1 $\mu$m window to the peak of the 1.18 $\mu$m window is very sensitive to water abundance (Figure 12). The short-wavelength side of the 1.18 $\mu$m region is also relatively unaffected by terrestrial water absorption, as it contains many high-J transitions of Venus water which arc much stronger and broader than their terrestrial counterparts. This makes it an ideal spectral region for probing the abundance of water vapour in the Venus lower atmosphere.

The peak of the 1.18pm window is most sensitive to water closest to the surface, while the flanks of the window probe higher altitude regions. Our radiative modelling results indicate that the peak of the window has a sensitivity function peaked near $\sim$ 11 ktn altitude, in agreement with the sensitivity functions determined by Pollack *et al.* (1 *993).* The sensitivity function, however, is broad, and the half-power points span 5 20 km altitude. This altitude range samples the bulk of the Venus atmosphere. In addition, although the window is dominated by emission from 11 km altitude, it is still sensitive to surface radiation, as is amply demonstrated by our 1.18 $\mu$m images which distinguish infrared emission from surface regions as little as 1 km above the mean elevation (Figure 7).

Here we describe a new technique for determining the water vapour abundance and distribution in the lowest scale height which provides improved vertical resolution. This method exploits the sensitivity of the 1.18 $\mu$m window to water vapour in the lower atmosphere, and uses our knowledge of the underlying surface topography to vary the column depths across the planet. '1'0 improve the vertical resolution, the column abundances above topographic regions with different elevations are compared, and differential column abundances between these elevations are inferred. This technique requires maps of the surface topography as well as spatially resolved spectra of the deep atmosphere.

Water maps for this analysis were derived from the IRIS data as follows. Two images were extracted from the fully flux-calibrated, but non-cloud-corrected cube, within the 1.18 $\mu$m window. The nominal 'water' image was extracted from within the 1.173 $\mu$m water absorption hand, with the chosen IRIS pixels spanning a manifold of lines within the wavelength range 1.1712-1.1755 $\mu$m. This image contains contributions to the absorption from both $H_2O$ and $CO_2$. The second, or '$CO_2$', image was chosen from a spectral range with a

comparative intensity on the long-wavelength side of the window, which contains no water absorption and is dominated by $CO_2$ absorption. The spectral region chosen spans 1.1897 1.939 $\mu$m. The water image is divided by the $CO_2$ image to create ratio maps which can be used to determine water distribution.

There are several advantages to this procedure. As cloud physical properties vary only slowly with wavelength, the ratio maps produced by the above method are relatively insensitive to differences in cloud opacity, which are of order 1 % between the spectral regions compared here. The water maps therefore do not require cloud-correction. The ratio also works to cancel most of the effects of $CO_2$ absorption on the water maps. To analyst the water maps, SMART and VENRAD are used with an assumed temperature lapse rate of $-8$ K/km and a uniform surface emissivity of 0.85, to create synthetic radiance maps in identical spectral ranges to the data maps. The synthetic water and $CO_2$ maps are then ratioed for comparison with the data. Subject to the accuracy of the data/model fit, this method reduces any effects in the data ratio maps associated with incorrect cancellation of the effects of $CO_2$ in the two regions chosen for the ratio. However, systematic errors in the inferred water abundance can occur when using this method, due to inaccuracies in the model fit to the data, especially on the steep, long-wavelength side of the window. These inaccuracies could occur either in the model, or in the wavelength and radiometric calibration of the data.

Water distribution maps derived from the data, and several model maps for different water abundances and near-surface gradients are shown in Figure 13. All models use the same $H_2O$ abundance above the cloud Last [32]. Model results are shown for uniform mixing ratios of 30 and 15 ppm in the lower atmosphere. The other model map shows a mixing ratio distribution of 25 ppm between the cloud base and 20 km altitude, and then increasing linearly to 50 ppm at the surface.

Figure 13 shows that contrasts observed across the Venus disk are very sensitive to both the total water abundance and mixing ratio gradient. The changes in observed contrast are due to two competing effects. At the surface, the decreasing temperature with altitude would create dark highlands in the ratios, as the ratio of the blackbody flux on the short and long wavelength side of the window is higher for objects at higher temperatures. Without the effects of water absorption, the hot lowlands would display a higher ratio value in these maps than the cooler highlands, and the highlands would appear dark on these ratio images.

The presence of water vapor absorption has the opposite effect on these ratios, however. The highlands would be bright, because the atmospheric column above them is shorter, and contains less water absorption at wavelengths near 1.173 $\mu$m. The lowlands are below a longer atmospheric column, and the increased water absorption in the longer column makes the lowlands appear darker in the ratio. The observed contrast between highlands and lowlands is a balance between the competing effects of temperature decrease with altitude, and differences in total water absorption in atmospheric columns above a range of topography.

We now consider the effects of a change in the mixing ratio of water with altitude. If the mixing ratio of water decreased from the surface upwards, then the increased abundance of water in the lowest few kilometres would work against, the temperature gradient effect, by darkening the lowlands and smoothing out the observed contrast due to temperature change

with altitude. A decrease in water mixing ratio towards the surface would work *with* the temperature gradient, brightening the lowlands when compared with the constant mixing ratio case. It is apparent qualitatively from Figure 13 tha L for the – 8.0 K/km lapse rate and a water vapor mixing ratio which increases towards the surface, that, t he contrast is reduced, and provides a better match to the data.

'1'0 provide quantitative verification of the water vapor distribution which provides the best fit to the data, the data ratio and model ratio are differenced. The resulting difference image was rebinned to create plots of the data-model difference as a function of altitude. In the binning process regions close to the crescent or affected by bad pixels are avoided, and a secondary radius is used to avoid all pixels within a given distance of the limb. Regions on the model maps for which no altimetry data exist were similarly avoided. However on the July 27 data this affects only a fcw limb pixels, which are rejected. To increase S/N, the following analysis uses altitude bins of 1 km.

## 6.5 The Water Gradient and Abundance in the lowest 6km

Figure 14 shows the resulting plot of the mean data-model difference as a function of altitude for several water abundances in the range 15 to 30 ppmv. A temperature lapse rate of −8K/km was assumed for these tests. For a perfect match to the data the difference of the data and model ratios should sit on the horizontal zero line. The model used to produce these results assumes no gradient in the lowest scale height. i.e. a constant water vapor mixing ratio throughout the lowest 20 km altitude. The points are placed in 1 km altitude bins, and the mean of the distribution within each bin is determined. These are the histogram values plotted. The error on this quantity is difficult to determine with a classical error analysis, as the data reduction aud analysis procedure used to derive this quantity is extremely complex. An estimate of the errors on the mean of the data-model difference is therefore determined by obtaining the standard error on the mean:

images has been determined by inspection to be accurate to within one IRIS pixel. Shifting the images by ±1 pixel produces no significant effect on the observed distribution.

The significant slope observed in the data/model difference as a function of altitude for the constant abundance models implies that a gradient dots exist in the lowest few kilometers. Although the weighting function for the atmospheric radiation peaks at 11 km for these wavelengths, and only ~ 25% of the observed emission originates from the planet's surface, the comparison of model and data is still very sensitive to the water gradient. This is demonstrated empirically in Figure 15 which compares the data with a number of different model gradients. A gradient in water vapour abundance is defined to be "negative" if the water vapour mixing ratio decreases towards the surface. On this diagram, if the model gradient matched the observations, then this would be seen as a straight line parallel to the altitude axis. Of the four gradients displayed, the model which most closely matches the observed behaviour of the data with altitude has a temperature lapse rate of –8 K/km and a water abundance of 30 ppm at 20 km, increasing linearly with pressure to 60 ppm at the surface. Mixing ratios which arc constant, or decrease with altitude, fail to match the data in the lowest few km. The strong negative gradient 30ppm above 16km altitude, decreasing to 15 ppm at the surface, produces the largest deviation from the data at low altitudes. Note also on this diagram that with the exception of altitudes of 6 km and over, it is still possible to distinguish between gradient differences as small as 30 ppm decreasing to 20 ppm and 30 ppm decreasing to 15 ppm, within the random errors displayed by the data. These results appear to contradict the negative water gradients inferred from the Pioneer Venus and Venera data (see TaMc 1).

Water absorption, however, is only one phenomenon that could change the observed emission. Surface emissivity, and the temperature lapse rate in the lower atmosphere, could also modify the data/model difference. To determine the impact of these effects on the water gradient determinations, models were run for a nominal 30 ppm water (constant mixing ratio) with a --8 K/km lapse rate, and a uniform surface emissivity of 0.85, and for comparison models with all other parameters nominal and alternately a temperature lapse rate of --7.5 K/km and a decreased surface emissivity of 0.75. The model/data differences for these cases are shown in Figure 16. Both the emissivity and temperature lapse rate changes produce very small effects on the estimated water abundance. The emissivity change produces a horizontal shift in the data-model comparison, implying a change in inferred absolute abundance rather than a change in gradient. However, the lapse rate change dots produce a small, but significant change in the behaviour of the model fit with altitude, with the decreased lapse rate resulting in a flattening of the observed gradient. This would be expected if the lower lapse rate decreased the temperature difference between the high and low altitude topography. However, for the 0.5 K/kin difference shown in the two models, the effect is much smaller than the effect produced by changing the water gradient. However, if the temperature lapse rate in the lowest 6 km was as much as a degree K less negative than the --8 K/km lapse rate, as is implied by the results discussed in the previous section, this would flatten the observed gradient, implying a more constant mixing ratio throughout the lowest scale height. A lapse rate several degrees below the nominal lapse rate in not physically precluded, as it could be produced through dynamical effects, which arc poorly

understood in the lower atmosphere. However, from the results presented in the previous section, it is unlikely that the lapse rate deviates from the nominal --8 K/kill value by more than 1 .(I degrees 1<.

The water results are shown in Figure 17. The three different plots show the effects of wavel engtlh calibration uncertainties in the data on the infered absolute abundance. The range of model results observed imply best fits of 22 ppm at 2(I km altitude, increasing to 44 ppm at the surface, 26 increasing to 52 ppm, and 29 increasing to 58 ppm. The results of this study therefore give a water abundance in the Venus lower atmosphere of $26^{+3}_{-4}$ ppm at 20 km, increasing by a factor of two to $52^{+6}_{-8}$ ppm at the surface. 1 lowever, this observed gradient is sensitive to the inferred temperature lapse rate. If the temperature lapse rate was substantially less negative than –8 K/km, then the inferred gradient would be much smaller, tending to a constant mixing ratio throughout the lowest scale height.

The absolute water abundance obtained with this new method is consistent with the 30 ppm obtained by previous remote. sensing results obtained by both ground-based observers, and the Galileo Near Infrared Mapping Spectrometer (cf. Table 2). However, this observation contradicts spacecraft data which indicate a negative gradient in water abundance. The only other existing determination of the water gradient in the lower atmosphere was derived from ground-based data [32]. The most likely result showed a constant absolute water abundance of 30ppm in the lower atmosphere.

As discussed by von Zahn *et al. (1983),* entry-probe data arc also subject to a number of measurement difficulties which can affect both the absolute abundance and the gradient observed. Both gas chromatography and mass spectromet cr measurements can be affected by the ingestion of $H_2SO_4$ cloud droplets. In addition, reactions between the gas inlet systems and calibration sources can produce extra water within the system, and water can also be adsorbed by the inlet system. Therefore large variations in measured abundance could occur, which may be at least partly due to instrumental contamination [1 4]. However, the in *situ* measurements made by the Venera 11 and 12 scanning spectrophotometers also show a negative gradient, and were unaffected by any of the instrumental problems which afflicted the mass spectrometers. Nevertheless, as in our method, the data require models in order to interpret the spectra obtained, Consequently the water abundances and gradient inferred may be non-u nique. The Venera data were independently analysed by Young *et al* [1984] who confirmed the original analysis by Moroz it et al. for the 0.94 $\mu$m water band, but reported discrepancies in the fit for water absorption at ().82 and 1.13 $\mu$m, which required a mixing ratio of 20 30 ppm for the entire atmosphere, rather than the 200 ppm decreasing to 20 ppm required by the 0.94 $\mu$m band. They suggested that an additional absorber may be responsible for the large equivalent width observed in the 0.94 $\mu$m band.

# 7 Summary and Conclusions

Using IRIS observations within the 1.0, 1.1, 1.18, 1.28 and 1.31 $\mu$m windows wc have confirmed model predictions that within the 1.0, 1.1, and 1.18 $\mu$m windows it is possible to

detect thermal radiation from the Venus surface. Given this result, these data provide an unprecedented opportunity to 1 ) search for infrared emissivity changes correlated with topography, 2) determine, and monitor changes in, the thermal structure of the lower atmosphere, especially as a function of local time, and iii) determine the water abundance and gradient in the lower atmosphere.

Methods were developed, taking advantage of the versatility of IRIS spectral mapping data, to correct for scattered light from the bright sunlit, crescent, which dominates the raw data. Methods were also developed to correct for the modulations in the observed emission that are produced when radiation from the surface and lower atmosphere passes through varying optical depths in the overlying cloud.

To analyze the data and achieve the above listed goals, sophisticated, angle-dependent radiative transfer models are combined with Pioneer Venus altimetry data to create 2-dimensional synthetic radiance maps, integrated over the same wavelength range as the data.

Synthetic radiance maps for the 1.18 $\mu$m were created with a uniform surface emissivity and were divided into data to look for variations in surface emissivity that may be correlated with topography. We find no evidence for infrared emissivity changes correlated with surface topography, or with the Magellan reflectivity data. This result confirms previous infrared results [24], and indicates that the process which produces the observed anomalous radar-reflectivity has no significant infrared signature.

The IRIS data also provide improved constraints on the vertical temperature gradient near the Venus surface. Comparison between IRIS data and synthetic radiance maps generated with SMART and VENRAD indicate that the temperature lapse rate is more stable than has previously been assumed. The stable near-surface temperature gradient could have important implications for the transport of momentum between the surface and the lower atmosphere, and for the efficiency of the atmospheric greenhouse mechanism. It also affects our efforts to retrieve water abundances at these levels.

To determine the water abundance and gradient in the lower atmosphere images extracted from within water vapour absorption lines were ratioed with spectral regions dominated by $CO_2$ absorption to produce maps of $H_2O$ distribution. Similar synthetic radiance maps were created within the identical wavelength regions used for the data, and for a range of water abundances and gradients. These data and model maps were differenced and these differences were binned as a function of altitude to explore the water abundance and gradient in the lower atmosphere. Despite the broad sensitivity function of water in the lower atmosphere, this method is very sensitive to changes in the vertical distribution of water, as it uses the altitude of known topographical regions to effectively vary the column depth that the water is sampled over, enhancing sensitivity to the water gradient in the lowest scale height.

The absolute water abundance at, the top of the lowest, scale height ($\sim$16 km) was $26^{+3}_{-4}$ ppm. This is consistent with previous ground-based spectroscopic results, and also with the results obtained by the Near-Infrared Mapping Spectrometer on board the Galileo spacecraft. However this abundance is not consistent with the much larger values obtained

by instruments on board entry-prolm spacecraft (rl'able 1). The gi adient determination yielded a surprising result. If the temperature lapse rate in the lowest scale height is near −8 K/km, then the IRIS data are best fit with models with a water vapour mixing ratio which increases by a factor of 2 towards the surface. However, if the temperature lapse rate is less than this, as is suggested by our thermal structure results, then a smaller gradient would be required. This result dots not agree with previous spacecraft observations which indicate a negative gradient in the mixing ratio near the surface. Entry-probe data are also subject to measurement difficulties, including sample contamination which can produce large variations in the measured abundance.

The total water abundance derived using this method supports the idea that global water content of Venus' lower atmosphere is c1osc to 30 ppm, as determined by previous ground-based observers. The lack of spatial variations observed in both this study, and the Galileo NIMS spectra, [1 6], also supports this conclusion.

This result constrains current models of the evolution of the Venus atmosphere, indicating a water amount that has a lifetime that is less than that of the solar system. It also constrains models of the surface/atmosphere interaction. It has been postulated that the surface of Venus may be covered with hydrated silicates, but recent calculations [17] suggest that these compounds would not be stable in atmospheric concenti ations of less than 100 ppm. Even with the slight increasing gradient in the water abundance measured here, the surface water abundance does not exceed 60 ppm and would appear to preclude the existence of hydrated silicates on the Venus surface.

The positive gradient in the water concentration revealed by this study also precludes the need for the complicated hydrogen replacement chemistry that had previously been required to explain the anomalous negative gradient observed by entry-~)robe spectrometers,

Finally, the water results have important implications for future Venus greenhouse models, as water is considered one of the three most important greenhouse gases in the Venus atmosphere. The relatively low abundance of water observed by these and other IR remote sensing observations requires modification of the existing models, and, when combined with the partial clearings in the cloud-deck observed in IR images, may indicate the presence of radiation leaks in the greenhouse. The positive gradient observed also has interesting implications for the thermal structure of the lower atmosphere by concentrating large amounts of thermally-absorbing compounds c1osc the the surface.

## Acknowledgements

This paper is dedicated with much gratitude to the memory of our collaborator Dr David Allen (1946 1994). David's discovery of the first near-infrared windows established this field of Venus exploration. His presence and guidance at the July 1991 observing run, and many of the subsequent runs were invaluable. We also thank him for many useful discussions throughout our years of collaboration. We will miss him.

This work represents partial fulfillment of the requirements for VSM's PhD degree at the University of Sydney, Australia. VSM was supported in part by an Australian Postgraduate Research Award and also acknowledges generous financial support from the Australian Feder-

ation of University Women-South Australia. The Anglo-Australia]) Observatory is thanked for allowing generous access to its computing and other facilities, and for the allocation of Anglo-Australian Telescope time. Part of this work was conducted at the Jet Propulsion Laboratory/California Institute of Technology, and supported by the NASA Planetary Atmospheres 1 'rogram and the Venus Data Analysis Program. This support is gratefully acknowledged.

## References

[1] D. A. Allen. The dark side of Venus. *Icarus*, 69:221 229, 1986.

[2] D. A. Allen. lAU Circ., 1990. 4962.

[3] D. A. Allen and J. W. Crawford. Cloud structure on the dark side of Venus. *Nature*, 307:222 224, 1984.

[4] J. F. Bell, III, D. Crisp, I'. G. Lucey, T. A. Ozoroski, W. A. Sinton, S. C. Willis, and B. A. Campbell. Spectroscopic observations of bright and dark emission features on the night side of Venus. Science, 252:1293 1296, 1991.

[5] B. Bézard, C de Bergh, D Crisp, and J. P. Maillard. The deep atmosphere of Venus revealed by high-resolution nightside spectra. *Nature*, 345:508 511, 1990.

[6] B. Bézard, C. de Bergh, J. P. Maillard, D. Crisp, J. Pollack, and I). Grinspoon. High resolution spectroscopy of Venus' night side in the 2.3, 1.7 and 1.1 1.3 $\mu$m windows. *Bull.* A7n. *Astron.* Sot., 23(3):1 192, 1991.

[7] R. W. Carlson, K. H. Baines, Th. Encrenaz, F. W. Taylor, P. Drossart, L. W. Kamp, J. B. Pollack, E. Lellouch, A. D. Collard, S. B. Calcutt, D. Grinspoon, P. R. Weissman, W. D. Smythe, A. C. Ocampo, G. E. Danielson, F. P. Fanale, T. V. Johnson, H. H. Kieffer, T.B. Matson, D. L. amd McCord, and L. A. Soderblom. Galileo infrared imaging spectroscopy measurements at Venus. *Science*, 253:1541-1548, 1991.

[8] R. W. Carlson, K. H. Baines, M. Girard, L. w. Kamp, P. Drossart, T. Encrenaz, and F. W. Taylor. Proceedings of the XXIV Lunar and Planetary Science Conference., 1993. pg 253.

[9] D. Crisp. Radiative forcing of the Venus mesosphere. I. Solar fluxes and heating rates. *Icarus*, 67:484-514, 1986.

[10] D. Crisp, D. A. Allen, D. H. Grinspoon, and J. B. Pollack. The dark side of Venus: Near-infrared images and spectra from the Anglo- Australian Observatory. Science, 253:1263 1266, 1991.

[11] D. Crisp, S. McMuldroch, S. K. Stephens, W. M. Sinton, B. Ragent, K. W. Hodapp, R. G. Probst, L. R. Doyle, D. A. Allen, and J. 1 'lias. Ground--based near-infrared

imaging observations of Venus during the Galileo encounter. *Science*, 253:1538- 1541, 1991.

*[12]* C. de Bergh, B. Bézard, T. Owen, D. Crisp, J. P. Maillard, and B. L. Lutz. Deuterium on Venus: Observations from Earth. Science, 251:547-549, 1991.

[13] C. deBergh, B. Bézard, D. Crisp, J. P. Maillard, T. Owen, J. Pollack, and D. Grinspoon. Water in the deep atmosphere of Venus from high-resolution spectra of the night side. in press, 1993.

[14] T. M. Donahue and R. R. Hodges, Jr. Methane measurement by the Pioneer Venus Large Probe Neutral Mass Spectrometer. In *Papers Presented to the International colloquium on Venus,* page *29, 1992.*

[15] T. M. Donahue! and R. R. Hodges, Jr. Past and present water budget of venus. *J. Geophys. Res.*, 97(E4):6083 6091, 1992.

[16] P. Drossart, B. Bézard, Th. Encrenaz, E. Lellouch, M. Roos, F. W. Taylor, A. D. Collard, S. B. Calcutt, J. B. Pollack, D. H. Grinspoon, R. W. Carlson, K. H. Baines, and L. W. Kamp. Search for spatial variations of the $H_2O$ abundance in the lower atmosphere of Venus from NIMS-Galileo. *Planet. Space Sci., 41(7):495-* 504, 1993.

[17] B. Fegley, Jr and A. H. Treiman. Chemistry of atmosphere-surface interactions on venus and mars. In J. Luhmann and Pepin. R. (). Treiman, editors, *Venus and Mars: Atmospheres, Ionospheres, and Solar Wind Interaction,* pages 7071, 1992.

[18] B. *G.* Gel'man, V. G. Zolotukhin, L. M. Mukhin, N. I. Lamonov, B. V. Levchuk, D. F. Nenarokov, B. P. Okhotnikov, V. A. Rotin, and A. N. Lipatov. Gas chromatography analysis of the chemical composition of the Venus atmosphere. Space *Res.*, 20:219, 1980.

*[19]* D. H. Grinspoon. implications of the high D/H ratio for the sources of water in Venus' atmosphere. *Nature,* 363:428-431, 1993.

[20] J. H. Hoffman, R. R. Hodges, Jr., M. B. McElroy, T. M. Donahue, and M. Kolpin. Venus lower atmospheric composition: Preliminary results from Pioneer Venus. Science, 203:800 802, 1979.

[21] V. G. Istomin, K. V. Grechnev, and V. A. Kochnev. Mass spectroscopy of the lower atmosphere of Venus: Krypton isotopes and other recent reults of the venera-1 1 and -12 data processing. *23rd COSPAR meeting-Adv. Space. Res., 1980.*

[22] [J. W. Kamp and F. W. Taylor. Radiative-transfer models of the night side of Venus. *Icarus*, 86:510 529, 1990.

[23] L. W. Kamp, F. W. Taylor, and S. B. Calcutt. Structure of Venus's atmosphere from modelling of night-side infrared spectra. *Nature*, 336:360 362, 1988.

[24] J. Lecacheux, I'. 1 Drossart, 1'. Laques, F. 1 Deladerriere, and F. Colas. Detection of the surface of Venus at 1.0 $\mu$m from ground-based observations. *Planet. Space Sci.*, 41(7):543 549, 1993.

[25] V. S. Meadows. PhD thesis, University of Sydney, 1994.

[26] V. S. Meadows, 1.). Crisp, and D. A. Allen. Ground-based near-infrared observations of the surface of Venus. In *Papers Presented to the International Colloquium on Venus*, pages 70 71, 1992.

[27] V. 1. Moroz. Panorama of the Venusian surface. some conclusions concerning boundary layer of atmosphere. *Kosmic. Issled., 14:691, 1976.*

[28] V. I. Moroz. Summary of preliminary results of the Venera 13 and Venera 14 missions. In D. M. Hunten, L. Colin, T. M. Donahue, and V. I. Moroz, editors, *Venus,* pages *45-68, 1983.*

[29] V. I. Moroz, B. E. Moshkin, A. P. Ekonomov, N. F. San'ko, N. A. Parfent'ev, and Yu M. Golovin. Venera 11 and 12 descent-probe spectrophotometry: the Venus daysidc sky spectrum. *Sov. Astron. Lett.*, 5(3):1 18-121, 1979.

[30] V. I. Oyama, G. C. Carle, F. Woeller, and J. B. Pollack. Venus lower atmospheric composition: Analysis by gas chromatography. Science, 203:802804, 1979.

[31] G. G. Pettengill, P. G. Ford, and R. J. Wilt. Venus surface radiothcrmal emission as observed by Magellan. *J. Geophys. Res.,* 97(E8):13091- 13102, 1992.

[32] J. B. Pollack, J. B. Dalton, D. Grinspoon, R. B. Wattson, R. Freedman, D. Crisp, D. A. Allen, B. Bézard, C. DeBergh, L. P. Giver, Q. Ma, and R. Tipping. Near-infrared light from Venus' nightside: A spectroscopic analysis. *Icarus, 103:1-42, 1993.*

[33] J. B. Pollack, O. B. Toon, and R. Boese. Greenhouse models of venus' high surface temperature, as constrained by Pioneer Venus measurements. *J. Geophys. Res.,* 85:8223-8231, 1980.

[34] H. E. Revercomb, L. A. Sromovsky, V. E. Suomi, and Boese. Net thermal radiation in the atmosphere of Venus. *Icarus, 61:521-538, 1985.*

[35] A. Stiff. Thermal structure of the atmosphere of Venus. In 1). M. Hun ten, L. Colin, T. M. Donahue, and V. I. Moroz, editors, *Venus*, pages 215-279, 1983.

[36] A. Seiff, D. B. Kirk, S. C. Sommer, R. E. Young, R. C. Blanchard, D. W. Juergens, J. E. Lepetich, 1'.1'. Intrieri, J. T. Findlay, and J. S. Derr Structure of the atmosphere of Venus up to 110 kilometers: Preliminary results from the four pioneer venus entry probes. *Science*, 203:787790, 1979.

[37] K. Stamnes, S. C. 'l'say, W. Wiscombe, and K. Jayaweera. Numerically stable algorithm for discrctc-ordinate-mcthocl radiative transfer in multiple scattering and emitting layered media. *Appl. Optics,* 27(1 2):2502-2509, 1988.

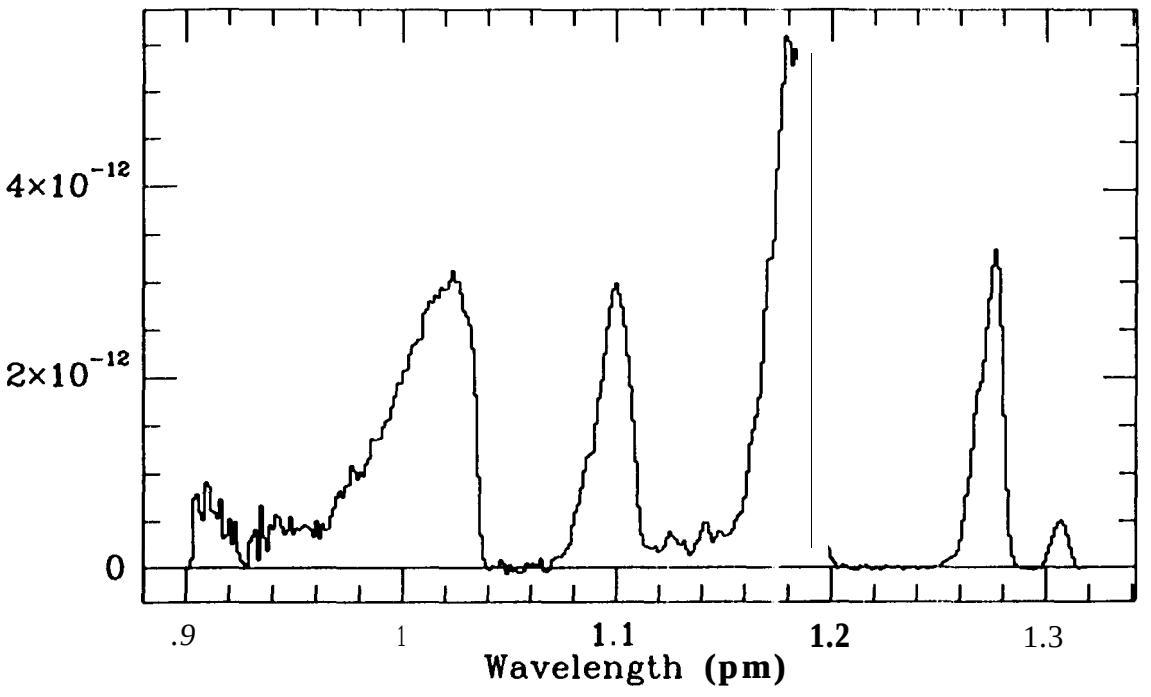


Figure 1: *Example of a fully-reduced IRIS spectrum of the* Venus *nightside within the spectral region 0.9-1.32 μm. This shows from left to right the 1.0, 1.1, 1.18, 1.28 and 1.31 μm windows. Intensity is shown in units of* $W m^{-2} \mu m^{-1}$.


*[38]* U. von Zahn, S. Kumar, H. Niemann, and R. Prinn. Composition of the venus atmosphere. In D. M. Hunten, L. Colin, T. M. Donahue, and V. 1. Moroz, editors, *Venus,* pages 299 430, 1983.

[39] R. B. Wattson and L. S. Rothman. Determination of vibrational energy levels and parallel band intensities of $^{12}C^{16}O_2$ by direct numerical diagonalization. J. *Molec. Spectrosc.*, 119:83-100, 1986.

[40] W. J. Wiscombe. improved mie scattering algorithms. *Appl. Opt.*, *19:1505-1509,* 1980.

[41] L. D. G. Young, A. T. Young, and L. V. Zasova. A new interpretation of the Venera 11 spectra of Venus. *Icarus*, 60:138-151, 1984.

[42] R. E. Young, R. L. Waltersheid, G. Schubert, A. Seiff, V. M. Linkin, and A. N. Lipatov. Characteristics of gravity waves generated by surface topography on Venus: Comparison with the VEGA balloon results. *J. Atmos. Sci.*, 44(18):2628- *2639, 1987.*

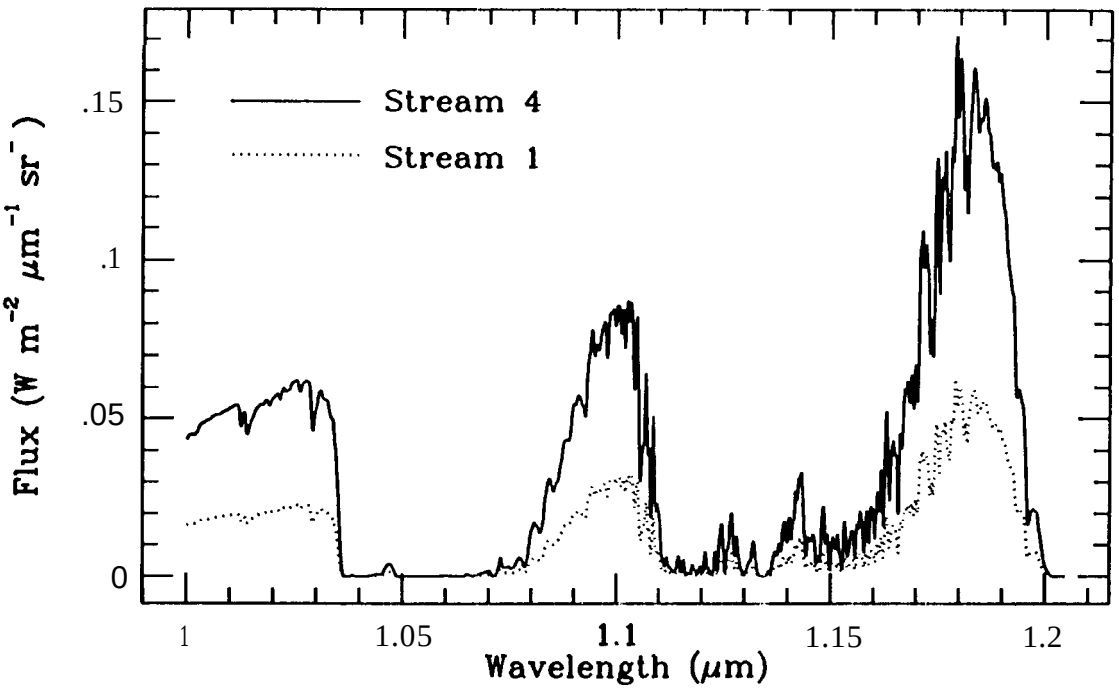


Figure 2: *An example of SMA RT output for two streams (i.e. two different viewing angles). The spectra. show the 1.0, 1.1 and 1.18pm windows. Stream* 4 *corresponds to a viewing angle of 22° (near the subearth point) and stream 1 shows the irradiance expected for observations at viewing angles of 86° (near the limb). The disparity in intensities between the two spectra is due to the strong limb-darkening suffered by the thermal radiation as it passes through* Venus' *dense atmosphere.*

Figure 3: synthetic *radiance map for wavelengths within the 1.18 μm window for October 1994. Venus is seen here at ∼ 0.25 phase, and the bright sunlit crescent is represented as the white area on the right of the disk. The dark* and *light patterns across the disk denote differences in infrared intensity induced by differences in surface temperature. Surface temperature varies as a junction of altitude, with highland regions on Venus* being *significantly cooler than the lowland plains. The large dark feature in the Northern hemisphere, near the centre of the disk, is produced by the highland region Beta Regio. The dark shape below it in the southern hemisphere is Phoebe Regio. The black regions at the poles of the planet show regions* where *Pioneer Venus altimetry does not exist, and synthetic radiances cannot be produced. The antisolar point, the point on the planet directly opposite the Sun, is marked as a small black cross near the left limb.*

FIGURE 3

Figure 4: *Diagram showing IRIS spatial maps of thermal emission observed within 5 near-infrared windo ws. For reference, an altitude map jor the date of the observation is shown at the bottom left. On the altitude map, high altitude regions have been set to appear darker than the bright surrounding plains. In this diagram, North on Venus is to the right, East at the top. Note the appearance of a dark oval feature in the 1.18, 1.1 and 1.0 μm images. The position of this feature* corresponds *closely to the geographical position of the highland plateau, Beta Regio, seen as a dark oval on the altitude map.*

Figure 5: *Sequence of IRIS images taken in October 1991. The three middle images show the 1.18 μm window on the 17th, 18th and 19th of October. These images are dominated by a dark equatorial feature which does not appear to move over the three day period.* For *comparison, images taken within the 2.3 μm window (bottom) show the cloud contrasts on the relevant days. The cloud images show changing patterns that are not seen in the 1.18 μm images,* and *the position of the 1.18 μm equatorial feature corresponds closely to Aphrodite Terra, seen 071 the model altitude images (top)*

Figure 6: *Horizontal variations in the optical depth of the overlying cloud will produce variations in the deep atmosphere radiation which are not predicted by the model. Therefore, before the data and model can be compared to derive information on the lower atmosphere, the cloud- induced contrasts must be removed. To do this, a scaled 1.31 μm image (which maps the cloud pattern, and shows no contribution from surface emission), is divided into the 1.18 μm image. The resultant cloud-corrected image now clearly shows contrasts in near-iii emission induced by differences in surface elevation.*

Figure 7: *Comparison of cloud-corrected images and synthetic radiance maps for the 1.18 and 1. 00 μm windows. The data are shown on the left, and the synthetic maps are shown on the right. The synthetic maps have been Gaussian smoothed to a FWHM of 1.2 arcseconds, to simulate terrestrial seeing.*

FIGURE 4

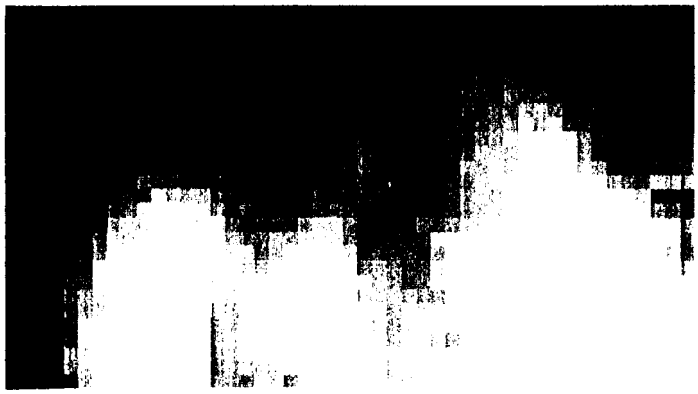

131 microns

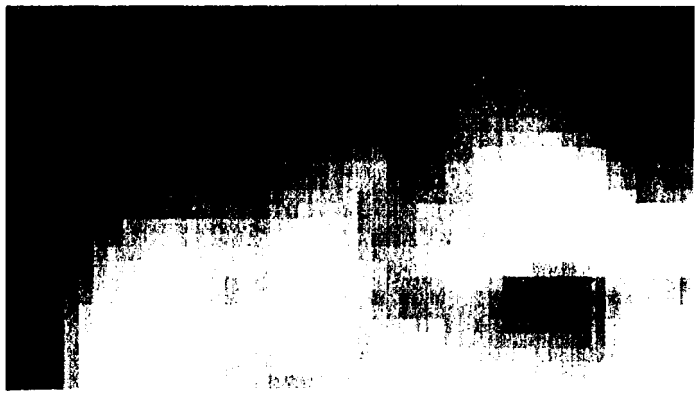

1.10 Hlici'oils

1.28 microns

1.00 microns

1.18 microns

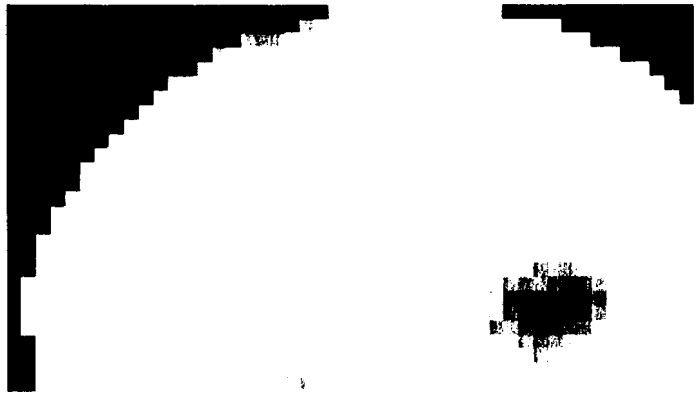

Surface Elevation

FIGURE 5

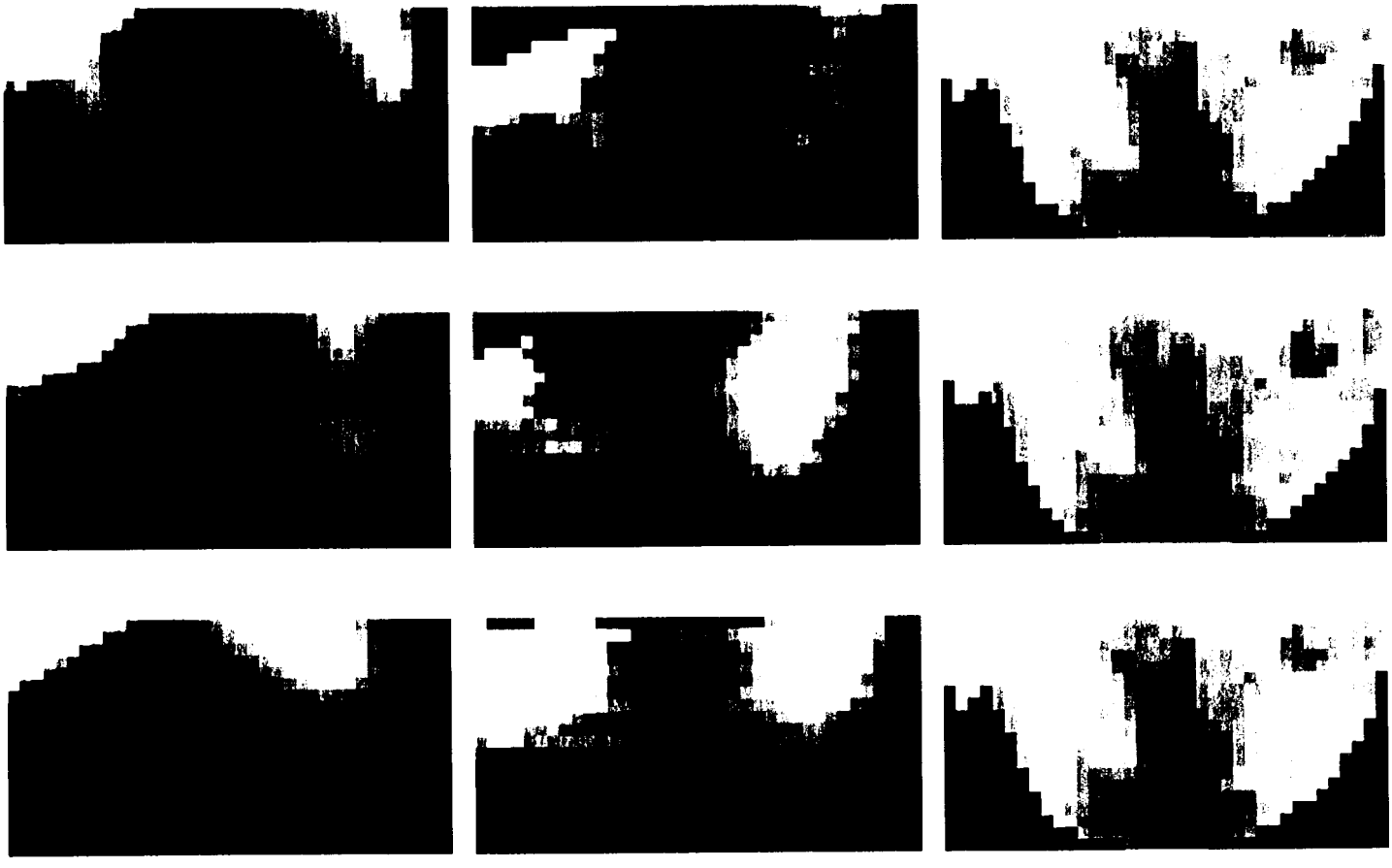

FIGURE 6

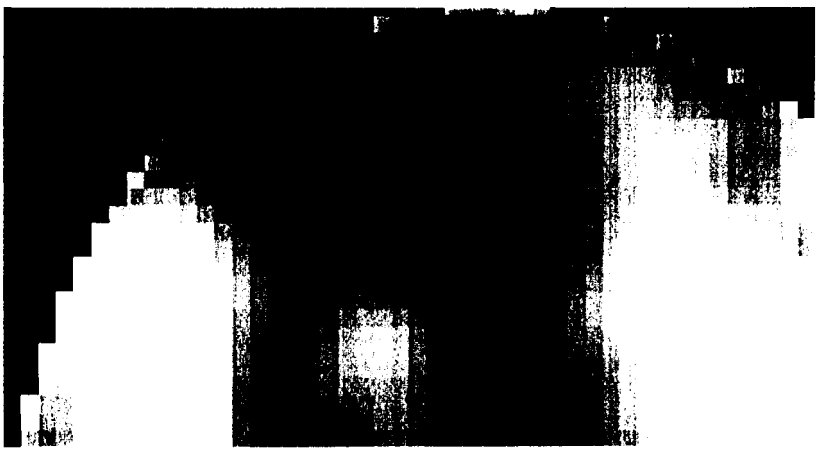

.31 micron image

1.18 micron image

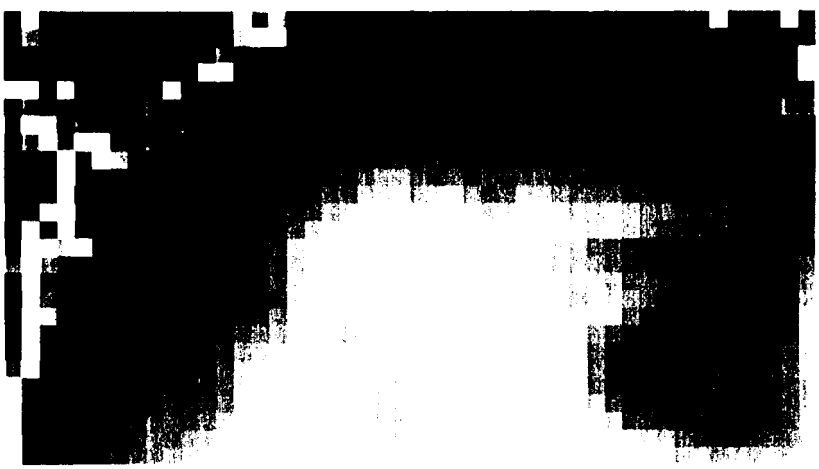

1.18/ 1.3 l micron image

FIGURE 7.

1.18 microns - IRIS data

1.18 microns - VENRAD model

1.00 microns - IRIS data

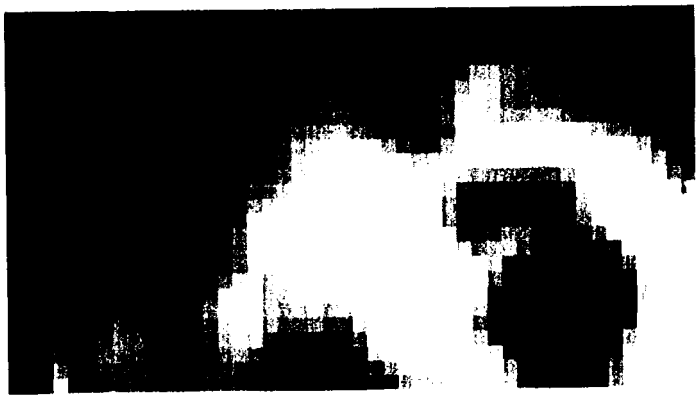

1.00 microns - VENRAD model

Figure 8: *Surface thermal emission contribution to emission within the Venus atmospheric windows. The solid line spectrum shows the radiative transfer modelling of the expected emission due to both the surface and atmosphere of Venus, within the 1.0 1. 31μm atmospheric windows. For comparison, the dotted line spectrum shows the emission expected from the atmosphere alone. 7'0 obtain this result, the surface temperature within the model was set to 1 K. The difference between these two spectra shows the expected surface contribution to the radiation observed within each atmospheric window. It can be seen that the surface is expected to contibute over 40% of the emission observed in the 1. 18μm window, over 60% in the 1.1 μm and over 95% of the radiation in the 1.00 μm window. in comparison, the 1.28 and 1.31 μm windows are expected to show little or no contribution from surface emission.*

Figure 9: *Test for surface emissivity variations. The top image shows the ratio of data divided by model within the 1.18 μm windows. The model image has been created with a uniform surface emissivity of 85%, nominal 30 ppm water abundance and a temperature lapse rate of – 7.5 K/km. For comparison, the model results are shown in the image below. In the model image, the high altitude topography can be clearly seen as darker regions. No spatial* **correlations** *with topography are detected in the data/model ratio.*

Figure 10: *Ratio of data and model for a – 7.5 K/km lapse rate as o junction of local time. Error bars show the 1 σ standard error on the mean of the distribution within each bin. For a perfect match between the model and data, the points would define a horizontal line with a value oj unity. In the 20 21 hour plot, scattered crescent light may affect the inferred gradient. Bins plotted with no error bars contain only one data point. This comparison suggests that a lapse rate of* – 7.5 *K/km, or smaller, is n ceded to fit the IRIS data.*

Figure 8

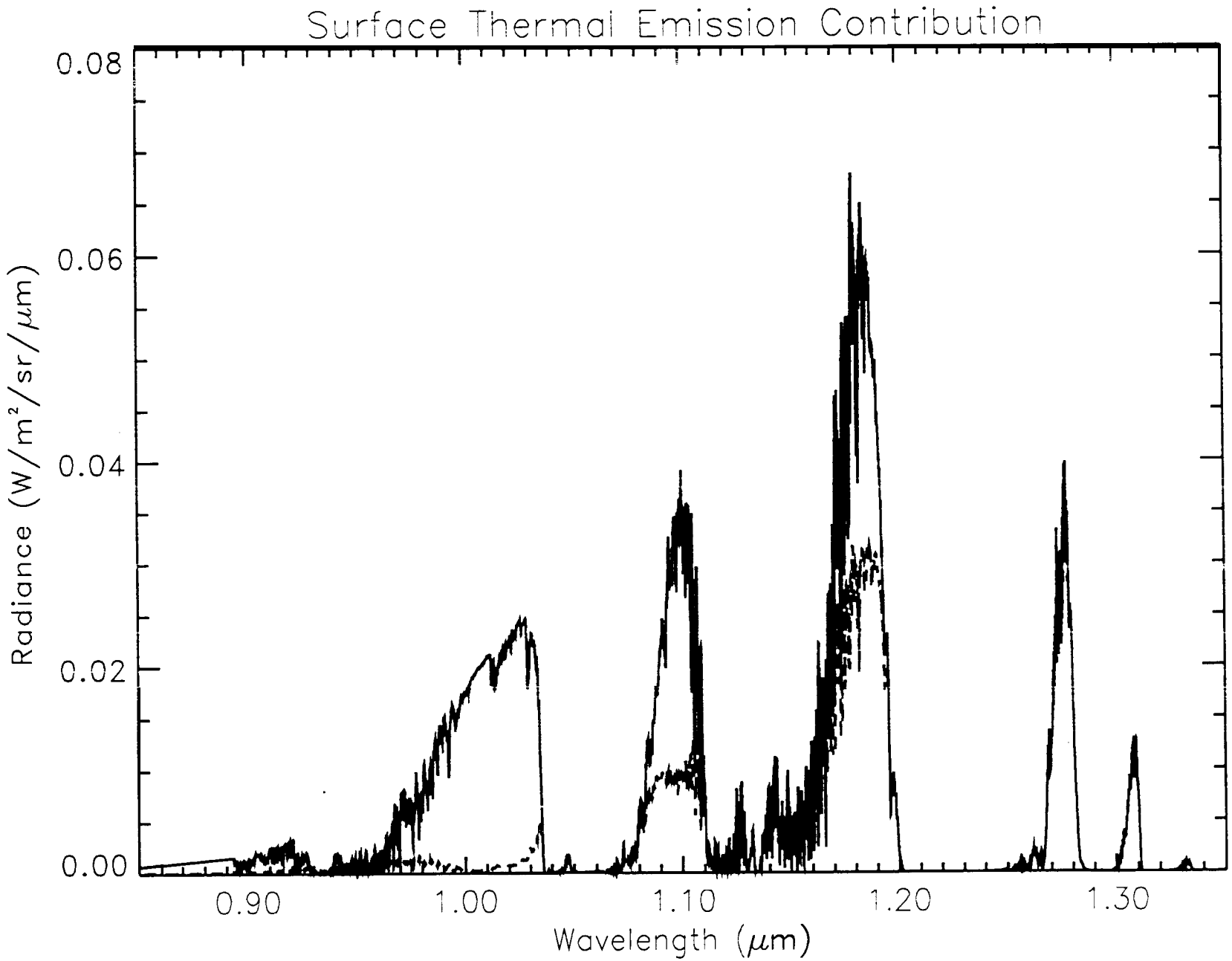
Surface Thermal Emission Contribution
0.08
0.06
0.04
0.02
0.00
Radiance (W/m²/sr/μm)
0.90
1.00
1.10
1.20
1.30
Wavelength (μm)

Figure 10

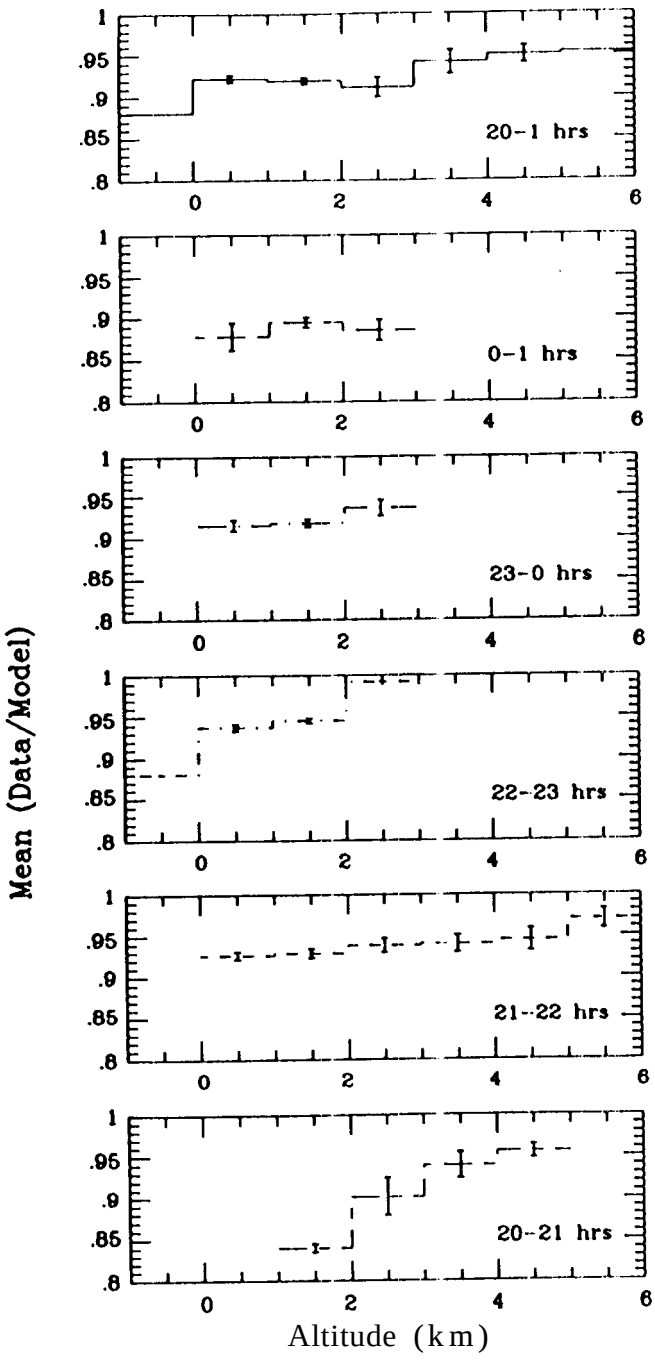
Mean (Data/Model)
1
.95
.9
.85
.8
0
2
4
6
20-1 hrs
0-1 hrs
23-0 hrs
22-23 hrs
21-22 hrs
20-21 hrs
Altitude (km)

Figure 11: *Ratio of data and model for a – 8.5 K/km lapse rate as a junction of local time. Error bars show the 1 σ standard error on the mean of the distribution within each bin. For a perfect match between the model and data, the points would define a horizontal line with a value of unity. In the .20-21 hour plot, scattered crescent light may affect the inferred gradient. Bins plotted with no error bars contain only one data point. This temperature lapse rate provides an inferior fit to the IRIS data, when compared with a temperature lapse rate of –- 7.5 K/km.*

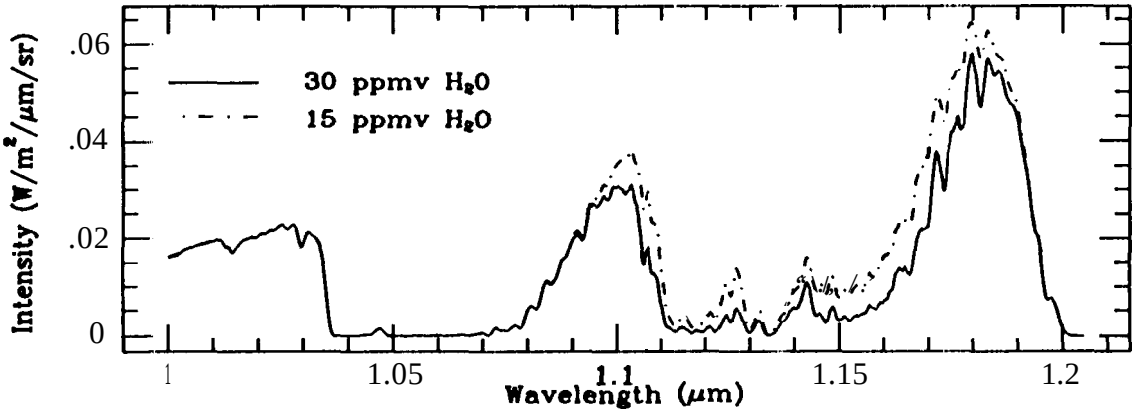


Figure 12: *Synthetic radiance spectra showing the sensitivity of the profiles of the 1.1 and 1.18 μm windows to variations in water abundance. Note in contrast that the 1.0 μm window, which is defined by strong $C0_2$ absorption, is completely insensitive to water abundance, as is much of the long wavelength side of the 1.18 μm window*

Figure 13: *Comparison of data ratio and the VENRAD ratio maps. The upper left image shows the ratio of the data jor images extracted within the wavelength ranges 1.1712 1.1755 μm (Water + $CO_2$) and 1.1897 1.1939 μm ($CO_2$). The other three images show the synthetic radiance maps for the same ratio. Clockwise from upper right, the ratio for a water abundance of 25 ppm at .20 km, increasing linearly to 50 ppm at the surface, the ratio for a constant 30 ppm water abundance, and the ratio for a constant 15 ppm water abundance. The increasing water gradient towards the surface serves to lessen the altitude contrast on these maps, providing a better match to the data.*

Figure 11

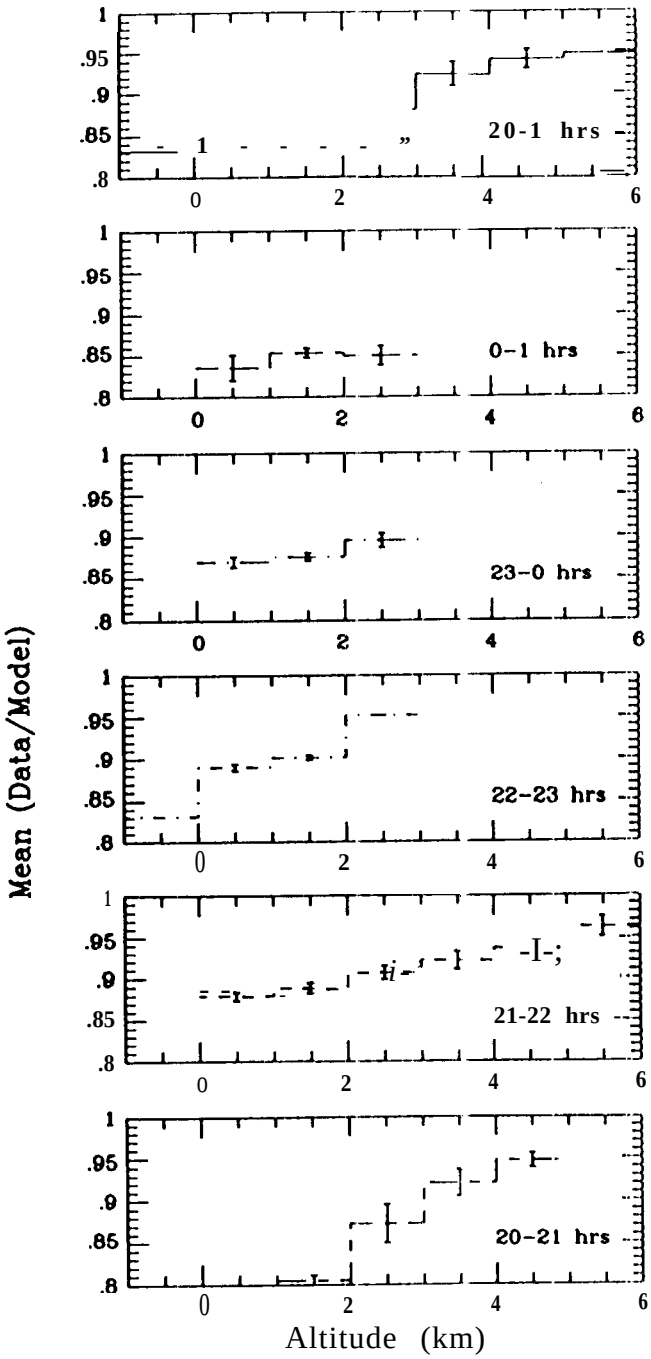
Mean (Data/Model)
20-1 hrs
0-1 hrs
23-0 hrs
22-23 hrs
21-22 hrs
20-21 hrs
1
.95
.9
.85
.8
0
2
4
6
Altitude (km)

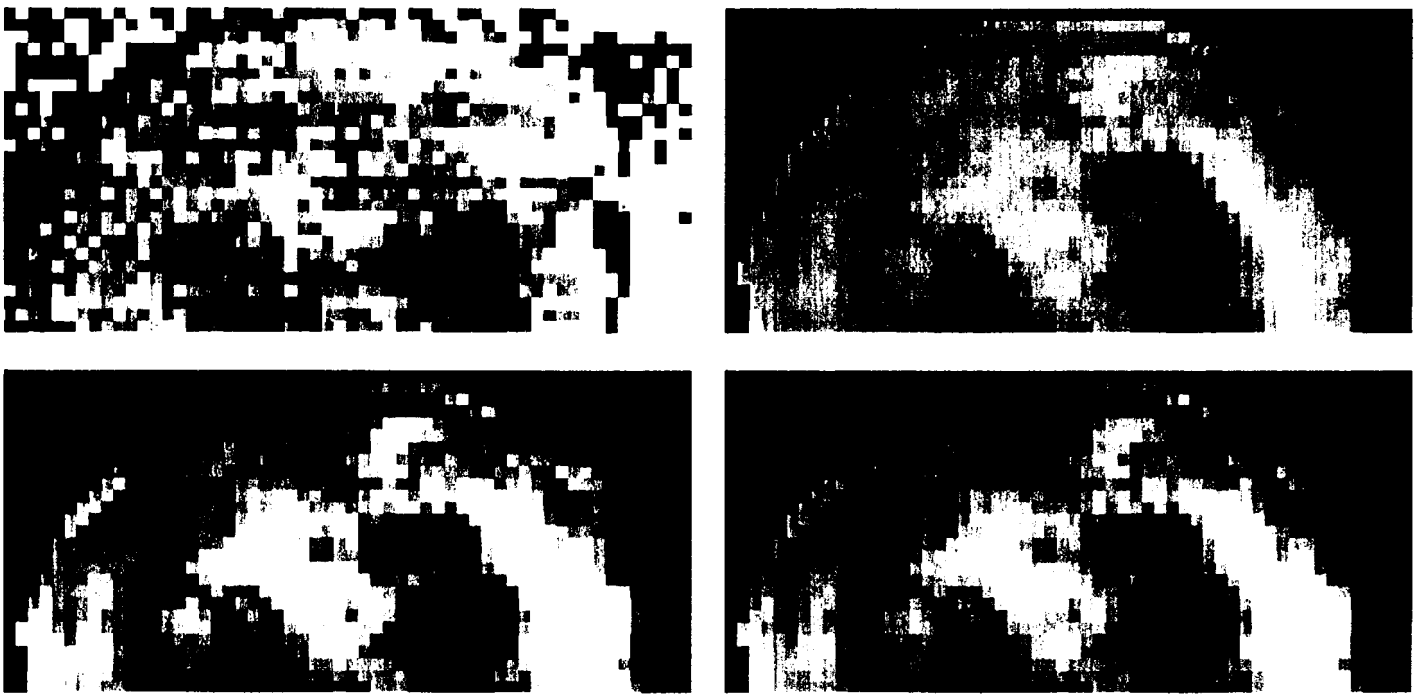

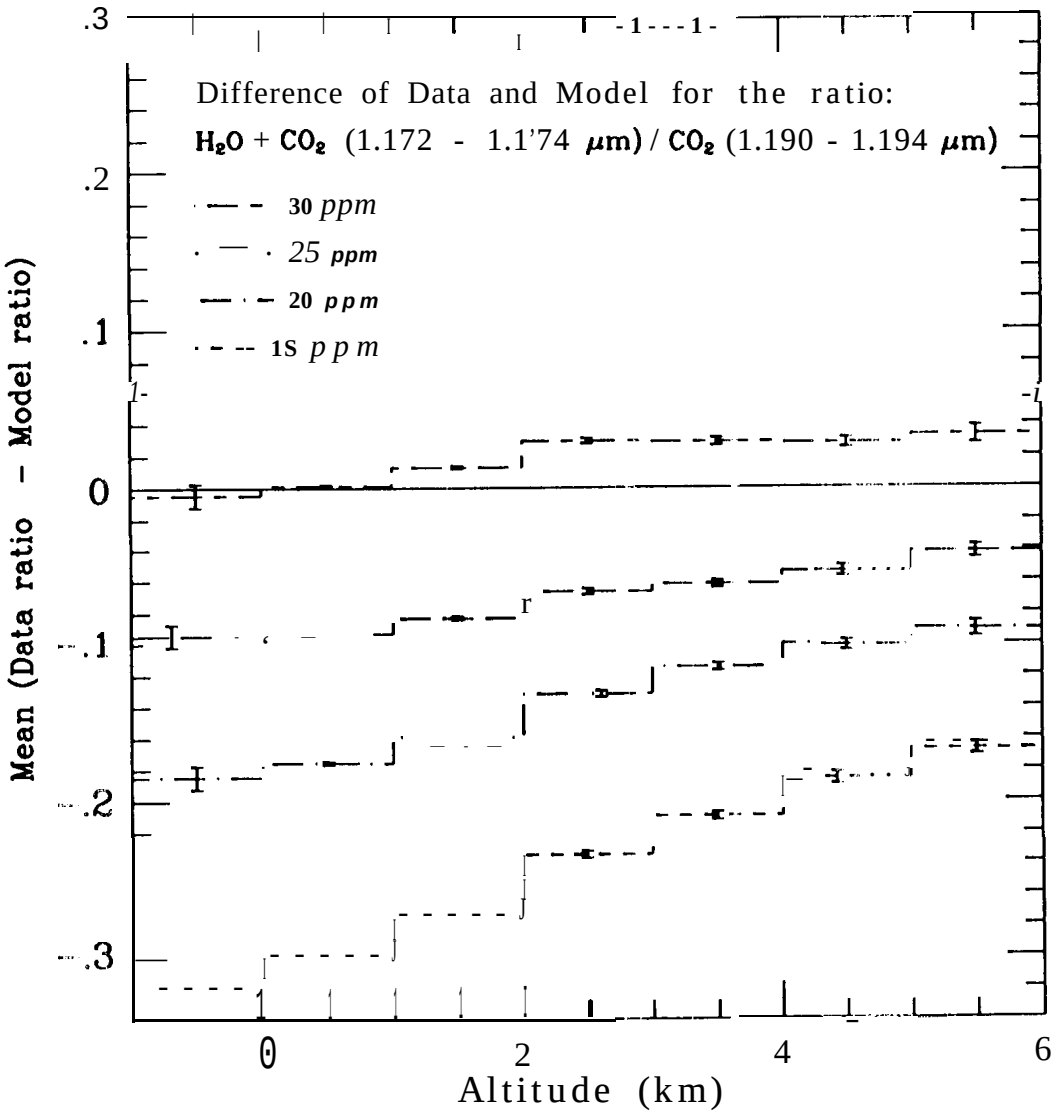


Figure 14: *Mean and standard error for the difference of data and model water maps as a junction of altitude. Comparisons for several constant mixing ratios in the range 15 to 30 ppm are shown. These model water gradients use a constant water mixing ratio of 30 ppm from the cloud base to 20 km altitude and then the constant mixing ratio indicated on the plot from .20 km down. to the surface.*

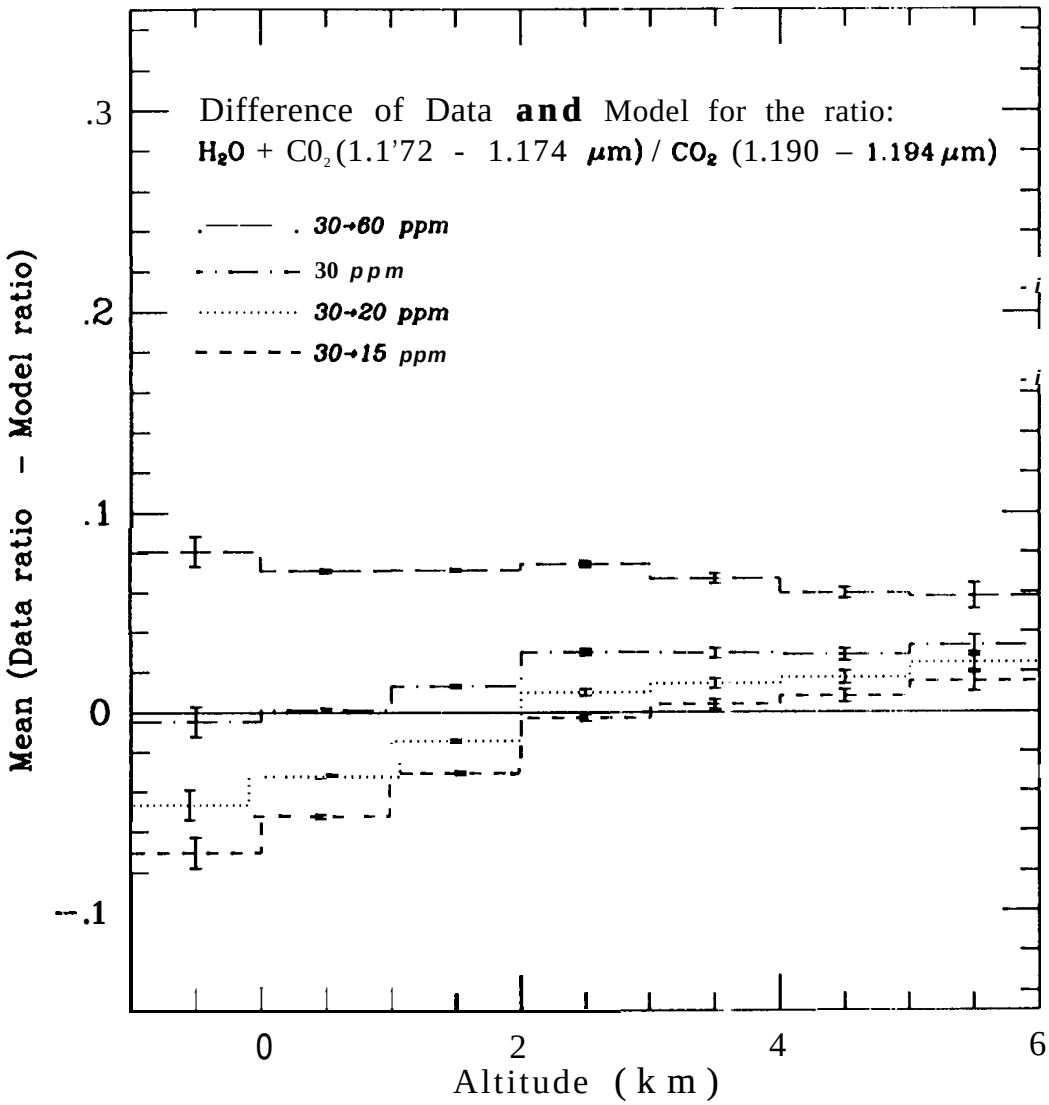


Figure 15: *Plot showing the sensitivity of the method to variations in the water gradient in the lowest 6 km of the Venus atmosphere. The error bars show the standard error on the mean for the difference of the model and data, binned in 1 km altitude bins. This plot shows the change observed for different water gradients. For a perfect gradient match to the data, the data/model difference should exhibit a straight line parallel to the altitude axis. For a constant mixing ratio of 30 ppm, and a decreasing gradient of 30 ppm at 20 km altitude, decreasing to 20 and 15 ppm at the surface, the data/model difference deviates significantly from a straight line behaviour with altitude. The best fit to the data is obtained with an increasing gradient in the water abundance from 20* **km** *to the surface.*

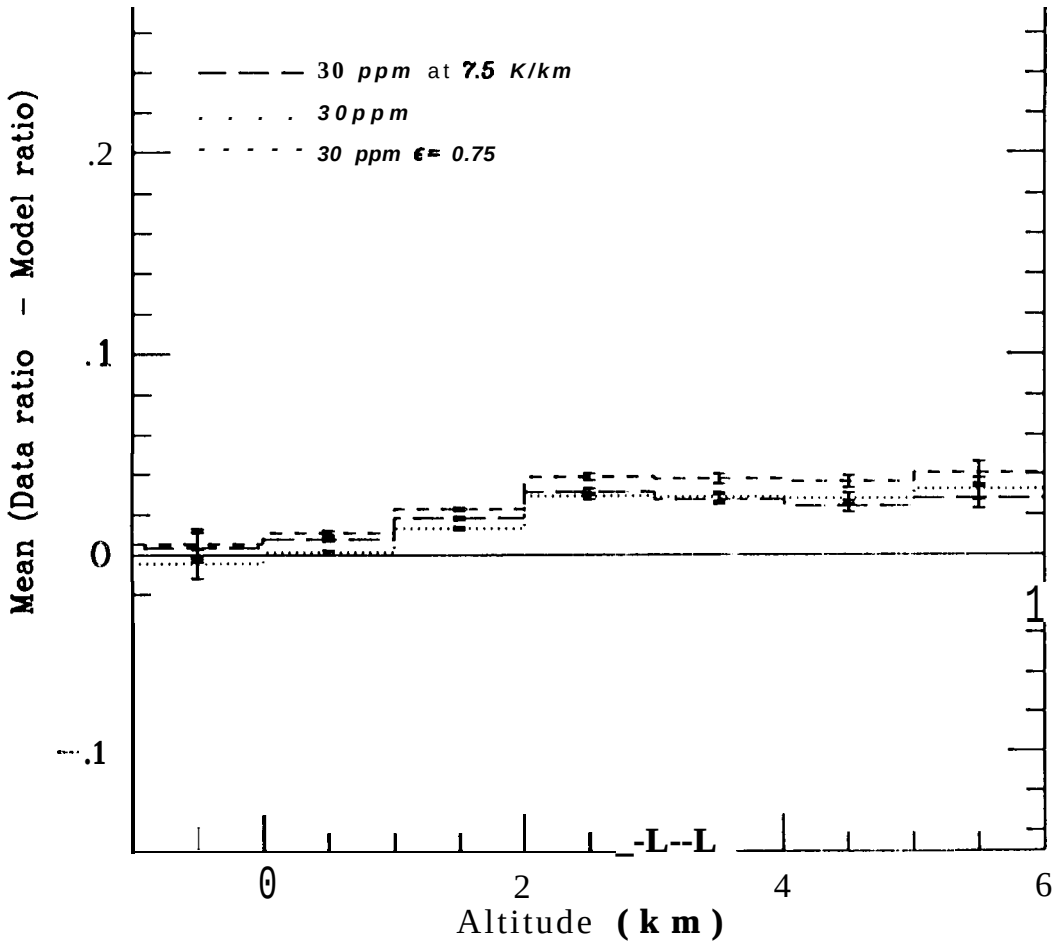


Figure 16: *Plot showing the sensitivity of the method to variations in the surface emissivity* **and** *temperature lapse rate. Variations in the surface emissivity principally produce a vertical shift on this diagram, implying a shift in the total water abundance, rather than any change in the inferred water gradient. The change in lapse rate however, can produce changes in the inferred gradient, although these have a much smaller effect than changes in the water gradient.*

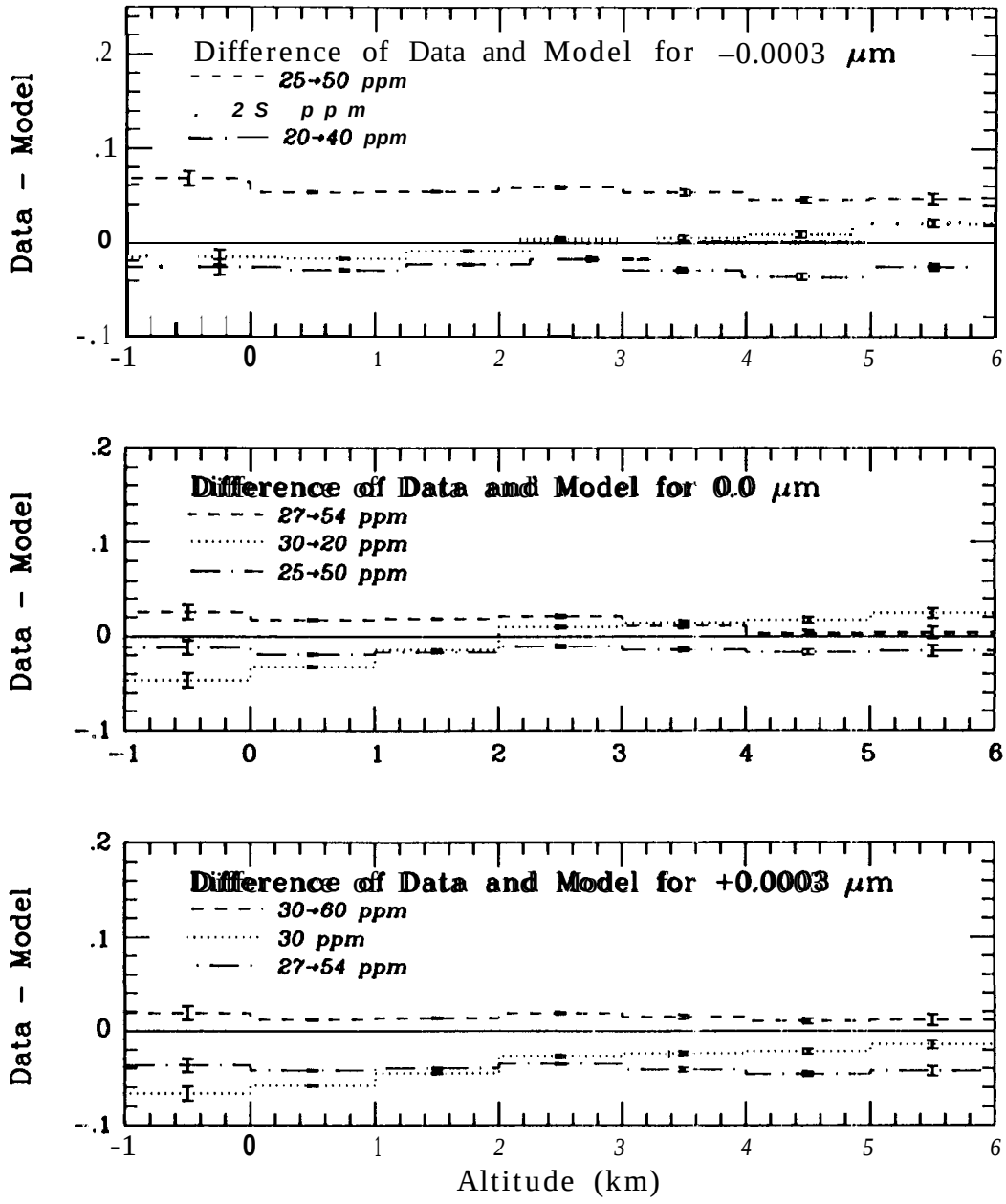


Figure 17: *Water abundance results. The three plots show the best fit models* **for** *the* **nominal** *correct wavelength calibration (0.0 μm), and the expected errors on either side of that position.*